

## Research Paper

# A developed soil reaction model for large-diameter monopiles in sand based on hyperbolic curves

Xiuyang Zhang, Degao Zou<sup>\*</sup>, Jingmao Liu, Kai Chen, Xin Li, Tianju Wang

The State Key Laboratory of Coastal and Offshore Engineering, Dalian University of Technology, Dalian, Liaoning 116024, China  
Department of Hydraulic Engineering, Dalian University of Technology, Dalian, Liaoning 116024, China

## ARTICLE INFO

## Keywords:

Large-diameter monopiles  
P-y curves  
Relative density  
Sand  
Pile side shear stress

## ABSTRACT

Given the preference as the foundation for offshore wind turbines, this paper focuses on large-diameter monopiles and presents a series of finite element analyses to investigate the response to lateral loads. The contribution of four soil reactions, including distributed lateral load ( $p$ - $y$ ), distributed moment ( $m$ - $\theta$ ), and base shear force and base moment, to the lateral resistance encountered by monopiles is quantified. It can be found that apart from the distributed lateral load, the contribution of distributed moment exceeds 14 %, while the proportion of base shear force and base moment is less than 5 % and is considered negligible. This research investigates how the diameter and embedded length of monopiles impact the load-bearing characteristics. A ' $p$ - $y + m$ - $\theta$ ' model based on the two-parameter soil reaction curve is proposed. This model is not only straightforward and easy to use for engineering design but also considers the effect of rotational deformation on the soil reaction curves. Additionally, a relationship between ultimate lateral soil resistance and relative density is established, leading to an analysis model suitable for sands of various relative densities. Finally, the model effectively predicts the load-displacement relationship for large-diameter monopiles under lateral loads, providing valuable support for monopile design in the offshore wind industry.

## 1. Introduction

As countries strive to reduce carbon emissions, offshore wind energy, recognized for its sustainability and renewability, has gained increasing significance. The Global Wind Energy Council forecasts a significant increase in offshore wind capacity, with an estimated 380 GW of new installations expected in the coming decade (GWEC, 2023). The foundation design plays a crucial role in the overall project, as it not only supports the wind turbine but also significantly impacts its performance (Hu et al., 2022). The cost of the foundation, including design, installation, and construction, typically accounts for 35 % to 55 % of the overall cost of an offshore wind project (Guo et al., 2022). Monopile foundations have emerged as the preferred choice for offshore wind projects in medium and shallow waters owing to their convenient installation and high cost-effectiveness (Amar Bouzid, 2018; Wang et al., 2022a). As offshore wind installed capacity expands, there has been a trend towards larger monopiles, with diameters reaching up to 10 m (Wu et al., 2019; Chen et al., 2023) and a length-to-diameter ratio ranging between 2 and 8 (Wang et al., 2022b). These monopiles can effectively withstand the load acting on the wind turbine at water depths

of up to 60 m. Specifically, monopile has proven successful in supporting the offshore wind turbines at Dogger Bank farm, the world's largest offshore wind farm, situated in water depths exceeding 63 m (Chen et al., 2023). In normal operation, offshore wind turbines must withstand these loads, such as self-weight, lateral forces, and moments generated by wind et al., as illustrated in Fig. 1(a).

Lateral forces and overturning moments are often the primary considerations in the design of monopiles, a fact underscored by studies like those of Hernandez-Estrada et al. (2021) and Chen et al. (2023). The  $p$ - $y$  method, known for its simplicity and efficiency as noted by Reese et al. (1974), is commonly employed for analyzing the bearing characteristics of laterally loaded piles, in agreement with industry standards such as API (2021) and DNVGL (2021). Essentially, this method transforms the laterally loaded piles into a nonlinear Winkler foundation beam model, employing a series of nonlinear springs to represent the soil's nonlinear response around the pile. The  $p$ - $y$  curve method, initially conceived for small-diameter flexible piles with a length-to-diameter ( $L/D$ ) ratio of about 34.4, was designed primarily for offshore oil and gas platforms. In contrast, when applied to laterally loaded large-diameter monopiles, particularly in the offshore wind industry where diameters exceed 4 m

<sup>\*</sup> Corresponding author.

E-mail address: [zoudegao@dlut.edu.cn](mailto:zoudegao@dlut.edu.cn) (D. Zou).

<https://doi.org/10.1016/j.compgeo.2024.106468>

Received 7 February 2024; Received in revised form 15 May 2024; Accepted 24 May 2024

Available online 31 May 2024

0266-352X/© 2024 Published by Elsevier Ltd.

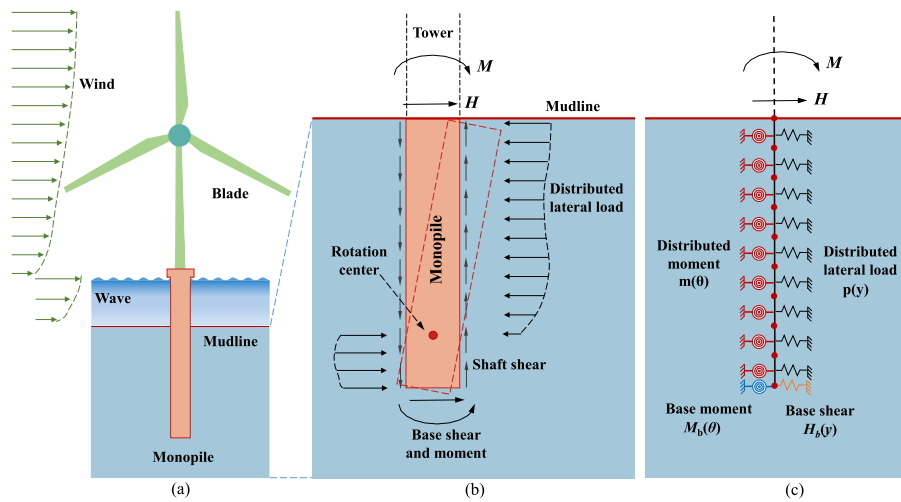


**Fig. 1.** Sketch of monopile foundation (a) Wind turbine under lateral loading (Byrne et al., 2020a) (b) Soil deformation mechanism of laterally loaded monopile (c) One-dimensional soil reaction model.

**Table 1**  
Summary of soil reaction models.

References	Distributed lateral load	Distributed moment	Base shear force	Base moment	Concentrated moment
Wang et al. (2020)	✓	—	—	—	—
Zhu et al. (2022)	✓	—	—	—	—
Liu et al. (2023)	✓	—	—	—	—
Zhu et al. (2022)	✓	—	—	—	—
Fuentes et al. (2021)	✓	—	✓	—	—
Zhang and Andersen (2019)	✓	—	✓	—	—
Cao et al. (2021)	✓	—	✓	✓	—
Fu et al. (2020)	✓	—	✓	✓	—
Byrne et al., (2020a)	✓	✓	✓	✓	—
Burd et al. (2020)	✓	✓	✓	✓	—
Jiang et al., (2022)	✓	✓	✓	✓	—
Lai et al. (2021)	✓	—	—	—	✓

**Table 2**  
Details for the numerical analysis.

Diameter $D$ (m)	Embedded length $L$ (m)	$L/D$	Load eccentricity (m)	Wall thickness $t$ (m)	Comment
4		7.5		0.046	—
6	30	5		0.066	—
8		3.75		0.086	—
10		3		0.106	—
8	40	5	5	0.086	$L/D = 5$
10		4		0.106	$D = 10$ m
10	50	5		0.106	$L/D = 5, D = 10$ m

and  $L/D$  ratios are lower than 10, it reveals that the methods recommended in current standards are insufficient. This inadequacy is evident as they fail to accurately predict the response of offshore wind turbines, as indicated by recent studies (Wang et al., 2020; Wang et al., 2022b; Zhang et al., 2023).

In recent years, scholars around the world have conducted numerous innovative centrifuge experiments (Klinkvort and Heddal, 2014; Zhu et al., 2015; Choo and Kim, 2016; Hong et al., 2017a; Zhu et al., 2017; Truong and Lehane, 2018; Byrne et al., 2020b; Mcadam et al., 2020; Wang et al., 2021b; Lai et al., 2022; Maatouk et al., 2022; Wang et al., 2022a) and numerical simulations (Achmus and Thieken, 2010; Amar Bouzid, 2018; Murphy et al., 2018; Otsmane and Amar Bouzid, 2018; Sun et al., 2020; Taborda et al., 2020; Wang et al., 2020; Zdravkovi C et al., 2020; Cao et al., 2021; Fuentes et al., 2021; Lai et al., 2021; Wan et al.,

2021; Wang et al., 2021a; Hu et al., 2022; Jiang et al., 2022; Wang et al., 2022a; Wang et al., 2022b; Chen et al., 2023; Zhang et al., 2023; Ma and Yang, 2024) aiming to enhance the understanding of the laterally loaded large-diameter monopiles. When comparing the sand  $p$ - $y$  curves obtained from these experiments and simulations with the API method, it is evident that the API method considerably overestimates the initial stiffness of the  $p$ - $y$  curves and underestimates the ultimate soil resistance (Wang et al., 2020; Fuentes et al., 2021; Wang et al., 2021b; Wang et al., 2022b; Zhang et al., 2023). This variation is attributable to the fact that the deformation mode of rigid and semi-rigid piles fundamentally differs from that of flexible piles, where the mode shifts from bending deformation to rotational deformation (Burd et al., 2020; Wang et al., 2020; Cao et al., 2021; Wang et al., 2022a; Wang et al., 2022b). Consequently, researchers have introduced various improvement methods to better suit large-diameter monopiles based on relevant experiments and numerical simulations. One approach focuses on refining the existing models by incorporating a depth-related correction factor into the original  $p$ - $y$  curve, thus enhancing its predictive capacity. Specifically, Thieken et al. (2015) derived a new  $p$ - $y$  approach which can give much better predictions through a comprehensive parametric study using three-dimensional numerical simulations. Wang et al. (2020) proposed a satisfactory  $p$ - $y$  curves based on the difference between the deformation patterns of large-diameter monopiles and small-diameter monopiles, taking into account the effect of the deformation mechanism on the ultimate lateral soil resistance. However, these methods are essentially modifications of the  $p$ - $y$  curve and still cannot completely describe the comprehensive pile-soil interaction due to changes in the monopile deformation modes, such as pile side friction, pile end shear, and

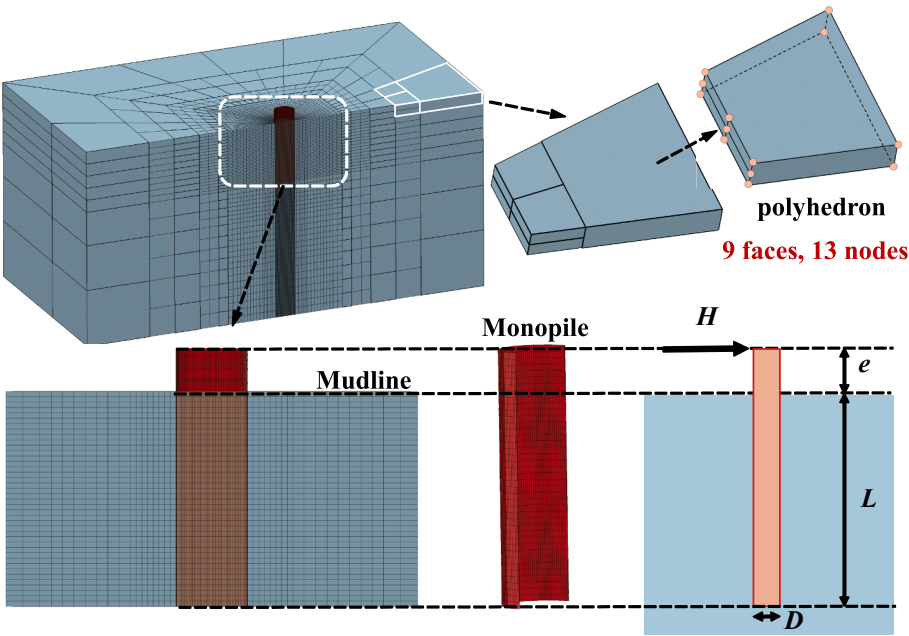


Fig. 2. 3D finite element mesh.

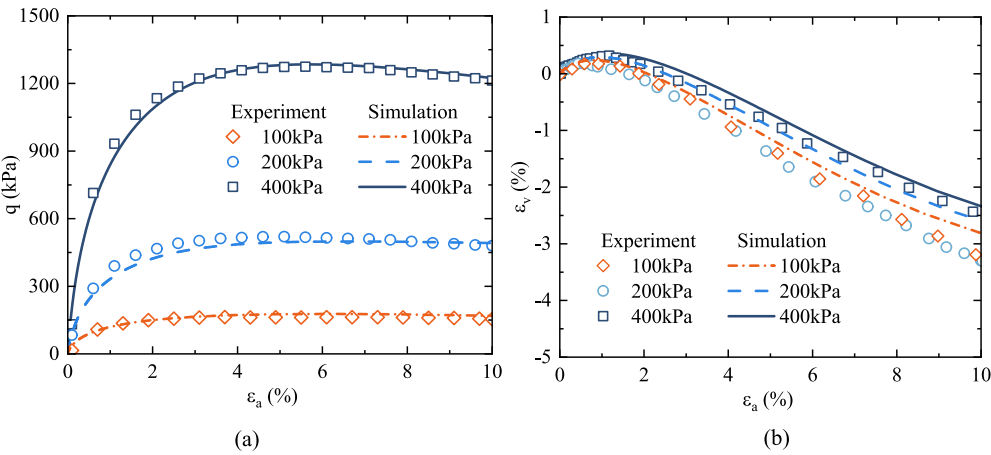


Fig. 3. Comparison between simulations and measured data (Taborda et al., 2020): (a)  $\epsilon_a$ - $q$ ; (b)  $\epsilon_a$ - $\epsilon_v$ .

Table 3  
Generalized plasticity model parameters for dense sand.

$G_0$	Elastic modulus			Plastic loading direction							Plastic modulus					
	$K_0$	$m_s$	$m_v$	$M_g$	$M_f$	$\alpha_g$	$\alpha_f$	$m_l$	$m_u$	$\gamma_{DM}$	$\gamma_d$	$\gamma_u$	$\beta_0$	$\beta_1$	$H_0$	$H_{u0}$
1053	1242	0.50	0.50	1.28	0.40	0.15	0.20	0.9	0.6	25	0.035	3.5	25	0.035	800	1200

Table 4  
Interface parameters between steel and sand.

$k_1$	$k_2$ (kPa/m)	$n$	$\varphi$
800	$1 \times 10^7$	0.5	27

moment. In contrast, another approach is proposed based on pile-soil interaction mechanisms (as shown in Fig. 1(b)), drawing from analysis methods for low  $L/D$  ratio foundations such as caisson foundations (Ashour and Helal, 2014; Karapiperis and Gerolymos, 2014). These methods extend the analysis by considering the effects of distributed lateral load, distributed moment, base shear force, and base moment and

suggest various computational models involving combinations such as two-spring (Zhang and Andersen, 2019; Fuentes et al., 2021; He and Kaynia, 2024) three-spring (Fu et al., 2020; Cao et al., 2021), and four-spring model (Burd et al., 2020; Byrne et al., 2020a; Jiang et al., 2022; Zhang et al., 2023) (as depicted in Fig. 1(c)), as detailed in Table 1. Moreover, Wang et al. (2020) proposed a two-spring model featuring a concentrated rotational spring located at the rotation center and distributed lateral load springs along with embedded length. The pile soil analysis (PISA) project utilized the four-spring model with four-parameter conic functions to describe four types of soil reaction curves. Despite its advances, the PISA model (Burd et al., 2020; Byrne et al., 2020a; Byrne et al., 2020b; Zdravkovi C et al., 2020), considering the influence of relative density, necessitates incorporating 39

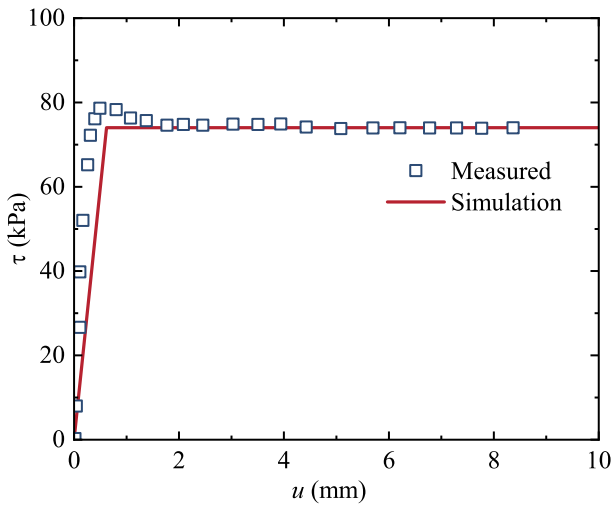


Fig. 4. Comparison between simulations and measured data for interface test (Said et al., 2009).

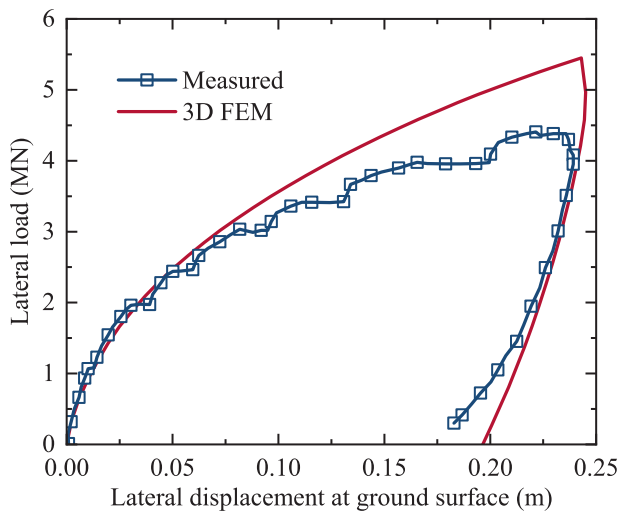


Fig. 5. Measured and FEM simulated load-displacement response at mudline (Taborda et al., 2020).

parameters, making it complex for engineering use and site-specific calibration. Moreover, it does not consider the impact of rotational deformation on the distributed lateral load. Additionally, the contributions of the four soil reaction components for monopiles with various  $L/D$  ratios have yet to be fully understood. Therefore, a systematic study is necessary to quantify the contributions of these components on the basis of the extracted soil reaction curves and to develop a simple pile-soil interaction model that is reasonable and convenient for engineering use.

This paper employs a validated three-dimensional refinement model to simulate the laterally loaded behavior of large-diameter monopiles with various diameters and embedded lengths. The contributions of four soil reactions to the lateral resistance of monopiles are quantified through the extracted soil reaction curves. Moreover, the influences of pile diameters and embedded lengths on the distributed lateral load and distributed moment are investigated. A novel method for determining the ultimate soil resistance and the initial stiffness is introduced, which accounts for the influence of rotational deformation modes by combining the calculation results of sand with different relative densities. A two-parameter soil reaction curve for the ' $p$ - $y + m$ - $\theta$ ' model is developed. Finally, the applicability of the model is confirmed by

applying it to the laterally loaded large-diameter monopiles.

## 2. Three-dimensional finite element analysis

A refined three-dimensional finite element model was developed for the monopile in the medium-dense sand, employing the geotechnical engineering finite element software GEODYNA for numerical simulation (Gong et al., 2020; Liu et al., 2020; Gong et al., 2021b; Qu et al., 2021; Nie et al., 2022; Qu et al., 2022; Gong et al., 2023; Liu et al., 2023). The validity of the finite element mesh and its constitutive parameters has been established through field experiments and centrifuge tests, as will be elaborated in the following subsection, "Validation of numerical methods". In this paper, the validated finite element mesh and constitutive parameters were utilized to examine the effects of diameters and embedded lengths on pile-soil interaction. The investigation covers the range of diameters and embedded lengths employed in current or planned offshore wind farms, with the details for the numerical analysis study outlined in Table 2. Specifically, to investigate the impact of embedded length, the monopile of diameter  $D = 10$  m and embedded length  $L = 40$  m or 50 m was selected, while the monopile with  $D = 8$  m and  $L = 40$  m was chosen to compare the load-bearing characteristics of monopiles with the same  $L/D$  ratio ( $L/D = 5$ ). Additionally, the wall thickness of the monopiles was determined according to the API standard, as specified in Eq. (1). Referring to the findings of Wang et al., (2022a), the loading eccentricity is not significantly impactful on the soil reaction curves. Therefore, all loading eccentricities are assumed to be 5 m.

$$t = 0.006 + \frac{D}{100} \quad (\text{m}) \quad (1)$$

In accordance with common practice in this field (Wang et al., 2020; Cao et al., 2021), the calculation and analysis employed the "wish-in-place" method of simulation while omitting the effects of monopile installation.

### 2.1. Constitutive model

The sand was modeled with the generalized plasticity constitutive model, originally introduced by Pastor et al. (1985). On this basis, Ling and Liu (2003) further considered the effect of stress level as well as densification behavior. Thereafter, this model was implemented and improved by Zou et al. (2013) and extensively employed in the analyses of geotechnical engineering such as nuclear power plant breakwaters, tunnels, and earth-rock dams (Gong et al., 2020; Liu et al., 2020; Ning et al., 2020; Gong et al., 2021a; Gong et al., 2021b; Qu et al., 2021; Qu et al., 2022; Liu et al., 2023). The constitutive model is described in the Appendix.

### 2.2. Finite element mesh and boundary conditions

Fig. 2 illustrates the 3D finite element mesh for a monopile with a diameter of  $D = 10$  m and embedded length  $L = 30$  m. To enhance computational efficiency, by exploiting the symmetry of the computational model and the loading conditions, only one-half of the pile is modeled. Furthermore, the efficient octree discretization technique is utilized for cross-scale modeling (Chen et al., 2021; Nie et al., 2022; Chen et al., 2023). This method ensures the refinement requirements for the mesh size around the monopile, simultaneously avoiding the extensive mesh generated by the traditional modeling method. The computation domain was chosen to be 20 times greater than the diameter of the monopile, and the depth from the pile toe to the bottom border is five times greater than the diameter of the monopile. Except for the transition elements simulated using high-precision scaled boundary finite element (Song and Wolf, 1997; Zhang et al., 2022), both the remaining soil and the monopile are simulated using eight-node hexahedral elements. The mesh comprises 125,643 elements, and models

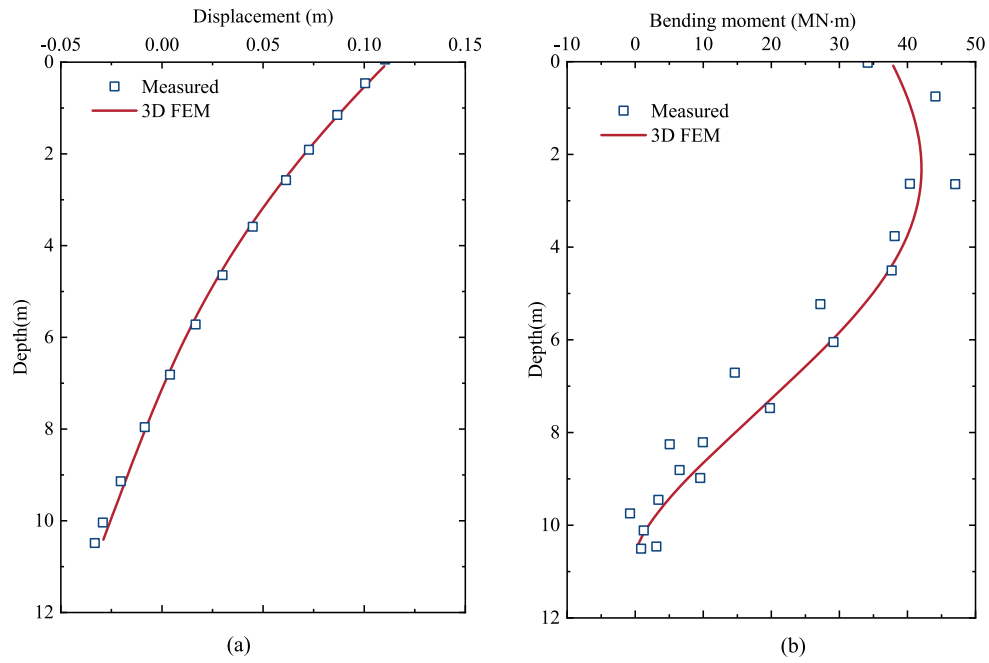


**Fig. 6.** Measured and FEM simulated lateral behavior (Taborda et al., 2020) (a) displacement profile corresponding to a ground-level displacement of 0.11 m (b) moment profile corresponding to a ground-level moment of 38.1 MNm.

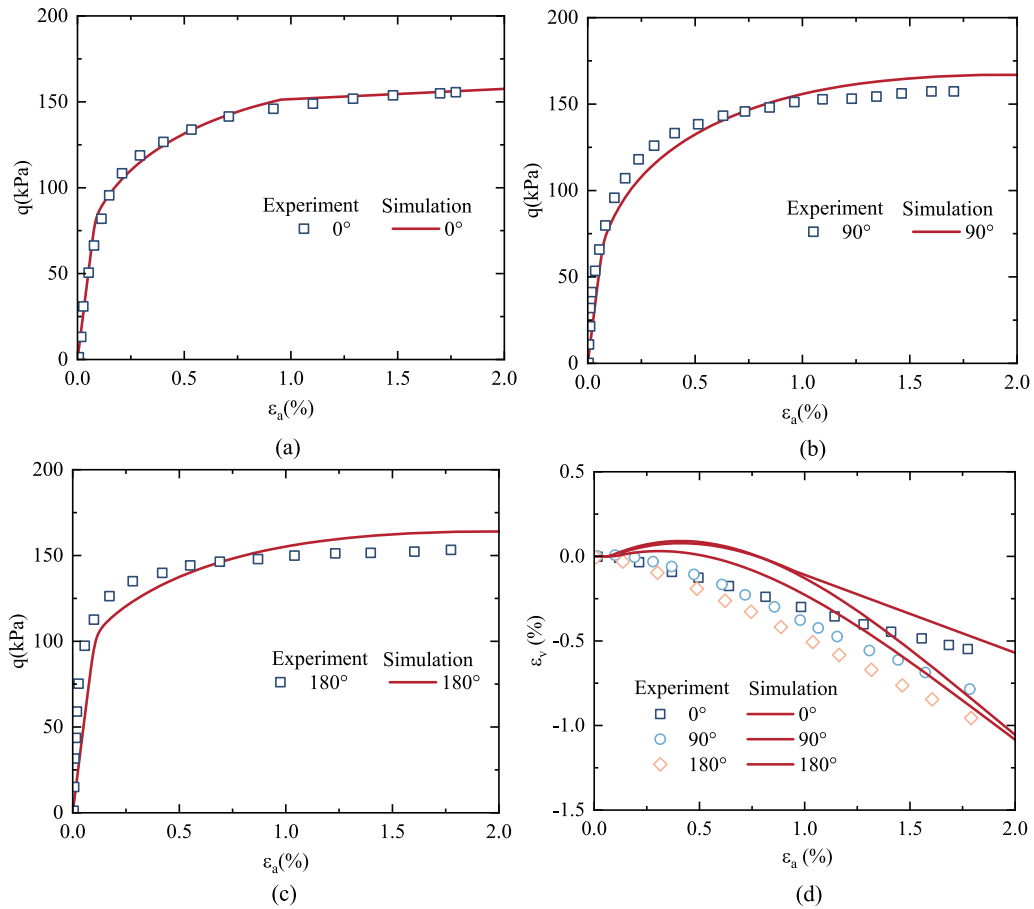


**Fig. 7.** Comparison between simulations and measured data for Toyoura sand (Hong et al., 2017b): (a) – (c)  $\varepsilon_a$ - $q$  (d)  $\varepsilon_a$ - $\varepsilon_v$ .

**Table 5**  
Generalized plasticity model parameters for Toyoura sand.

$G_0$	Elastic modulus			Plastic loading direction							Plastic modulus					
	$K_0$	$m_s$	$m_v$	$M_g$	$M_f$	$\alpha_g$	$\alpha_f$	$m_l$	$m_u$	$\gamma_{DM}$	$\gamma_d$	$\gamma_u$	$\beta_0$	$\beta_1$	$H_0$	$H_{u0}$
330	245	0.50	0.50	1.25	0.81	0.85	0.4	0.7	0.6	25	0.035	3.5	30	0.02	1300	1500

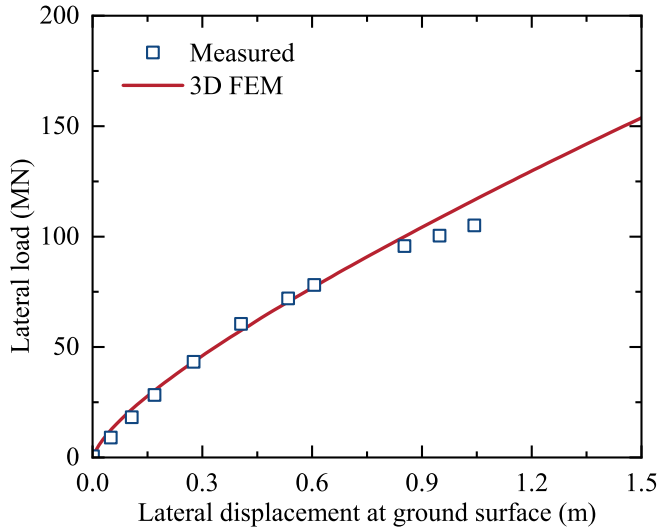


**Fig. 8.** Measured and FEM simulated load–displacement response at mudline (Wang et al., 2022a).

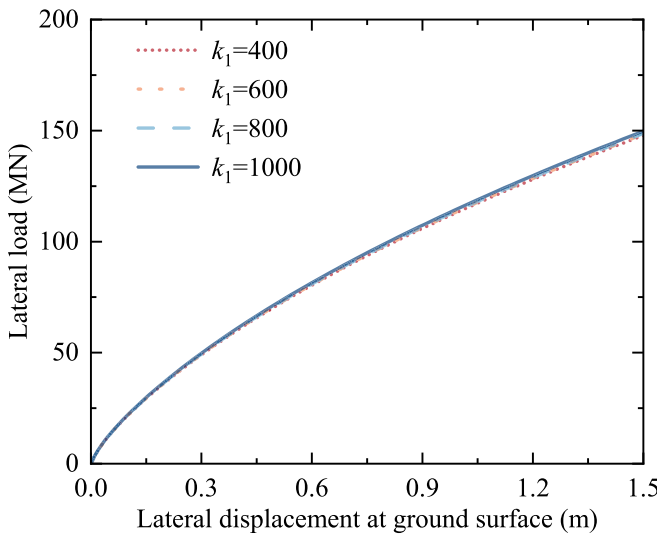


**Fig. 9.** Computed load–displacement curves at mudline with different  $k_1$ .

with different pile diameters are modeled with identical mesh densities. The bottom of the model uses a pinned boundary, while the lateral boundaries employ lateral constraints.

### 2.3. Pile-soil interface

The interaction between the pile and the soil is simulated by the pressure-dependent perfect elastoplastic interface model (Zou et al., 2013). The shear stiffness and normal stiffness are determined as follows:

$$k_{zx} = k_1 p_a \left( \frac{\sigma_z}{p_a} \right)^n, \tau < c + \sigma \tan \varphi \quad (2)$$

$$k_{zy} = k_1 p_a \left( \frac{\sigma_z}{p_a} \right)^n, \tau < c + \sigma \tan \varphi \quad (3)$$

$$k_{zz} = k_2 \text{ under compression} \quad (4)$$

$$k_{zz} = 0 \text{ under tension} \quad (5)$$

where  $k_{zx}$  and  $k_{zy}$  represent the shear stiffness of the interface in the two directions, respectively;  $k_1$  represents the interface modulus coefficient;  $n$  represents the interface modulus index;  $k_2$  represents the compressive stiffness.

## 3. Validation of numerical methods

### 3.1. Field experiments of large-diameter monopile at Dunkirk

The PISA project (Burd et al., 2020; Taborda et al., 2020) performed field experiments on lateral loading monopiles at Dunkirk in France. This paper uses the CL2 rigid pile as a case to examine the effectiveness of the finite element model and constitutive parameters. The pile has a diameter of 2 m, a load eccentricity of 10 m, and an approximate  $L/D$  ratio of 5. According to the results of Taborda et al. (2020), it is known that the groundwater table is 5.4 m below the mudline, with the total unit weight of the sand over the water table being 17.1 kN/m<sup>3</sup> and below it, 19.9 kN/m<sup>3</sup>. The critical stress ratio of the sand is 1.28, and the elastic shear and bulk modulus coefficients are 1053 and 1242, respectively. Other parameters were calibrated based on the triaxial test, with the calibration results presented in Fig. 3 and the final computational parameters presented in Table 3. The monopile was simulated using an elastic material that has an elastic modulus of 200 GPa and a Poisson's ratio of 0.3. For the interface, the contact characteristics between the monopile and the internal and external soils were simulated using the perfect elastoplastic interface. These interface parameters were calibrated using the studies of Said et al. (2009). The perfect elastic–plastic interface model adopted in this paper, in fact, cannot capture the softening phenomenon that occurs in the test. In order to ensure the same initial shear stiffness (10<sup>5</sup> kN/m) as that used in the PISA project (Taborda et al., 2020) and to ensure the overall consistency of the test results, the parameters in Table 4 were finally obtained, and the fitting results are shown in Fig. 4.

Fig. 5 compares the computational results with the load–displacement relationship measured in the field at the surface. It becomes clear that before the lateral displacement of the mudline exceeds 0.11 m, the calculation results of the numerical simulation are in accordance with the experiment results. As can be seen from the figure, in the initial loading stage, the finite element numerical simulation results are very close to the test results. In the middle and late stages of loading, the creep effect leads to larger deformation in this stage. In this paper, like the calculation method of Wang et al. (2020) and Taborda et al. (2020), the influence of the creep effect has not been considered yet, so the deformation at the peak loading point is relatively small. In other words, if the creep effect is considered, the numerical simulation results of the whole loading stage will be more consistent with the test results. Fig. 6 presents a comparison between the simulated and measured lateral displacement and moment of the monopile. The displacement and



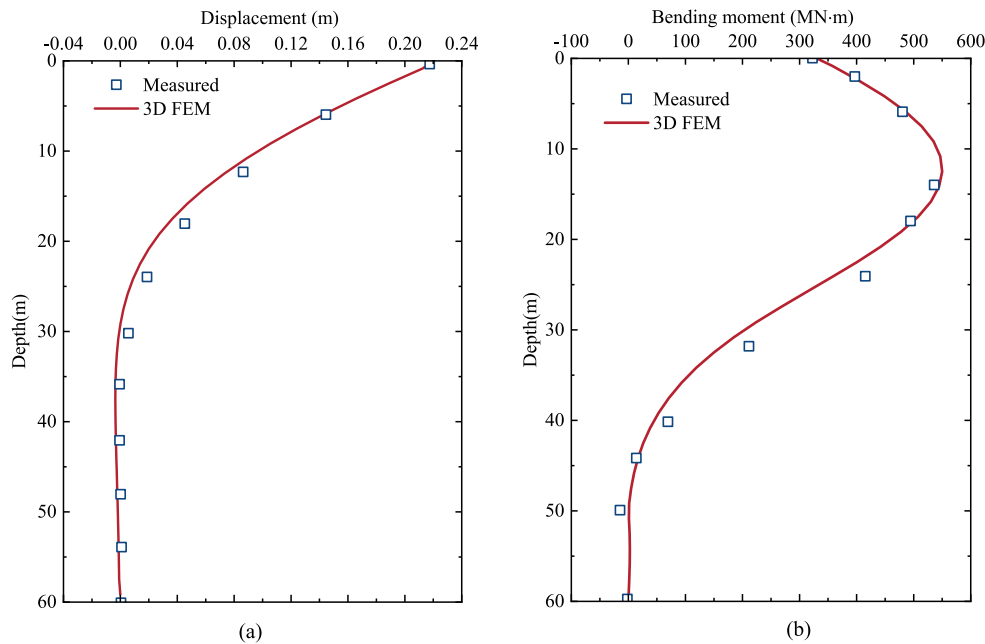


**Fig. 10.** Measured and FEM simulated lateral behavior (Wang et al., 2022a) (a) displacement profile corresponding to a ground-level displacement of 0.22 m (b) moment profile corresponding to a ground-level moment of 330 MNm.

bending moment along the embedded length demonstrate good consistency, thereby further demonstrating that the analysis method accurately captures the lateral loading characteristics of the monopile.

### 3.2. Centrifuge tests of medium-dense sand

The purpose of this case is intended to validate the analysis method by contrasting calculated responses with the centrifugal test of large-diameter monopile performed by Wang et al. (2022a). For this analysis, the prototype monopile has a diameter of 6 m and an embedded length of 60 m. The experiment was carried out on sand of 65 % relative density. The sand used is the international standard sand, Toyoura sand. Based on the research of Cen et al. (2018), the shear modulus coefficients and critical stress ratio were determined, while other constitutive parameters were calibrated based on the triaxial test data of Hong et al., (2017b). The simulation results for different stress path tests are shown in Fig. 7, where the angle  $\theta$  describes the directional angle in the  $p$ - $q$  space between the current and previous stress path directions; detailed calibration parameters are given in Table 5. The interface parameters were determined according to Table 4, and a sensitivity analysis of the interface tangential stiffness ( $k_s = 400, 600, 1000$ ) was conducted while keeping the normal stiffness and interface strength unchanged.

Fig. 8 presents the load-displacement behavior in the mudline calculated through finite element analysis, which closely matches the experimental results. In addition, this paper also analyzes the effect of the shear stiffness of the interface on the lateral loading characteristics of monopile, and the results in Fig. 9 of the manuscript show that there is basically no influence. Fig. 10 compares the numerical calculations with the measurements of lateral displacement response and moments across the embedded length. This comparison reveals good consistency throughout the embedded length, demonstrating that the analysis method can effectively represent the lateral load characteristics of the monopile.

## 4. Soil-monopile responses and development of soil reaction model

### 4.1. Soil flow mechanisms and the mechanism-based soil-pile interaction models

Results from centrifuge experiments (Hong et al., 2017a; Wang et al., 2021b; Lai et al., 2022; Maatouk et al., 2022; Wang et al., 2022a), field experiments (Zhu et al., 2017; Byrne et al., 2020b; Mcadam et al., 2020), and numerical simulations (Wang et al., 2020; Cao et al., 2021; Wang et al., 2022c) indicate that the aspect ratio ( $L/D$ ) of the monopile plays a crucial role in describing the soil flow mechanism and failure modes of the monopile. To validate and understand the failure modes of monopiles with different diameters, Fig. 11 presents the lateral displacement contour and vector field of monopiles with three different diameters ( $D = 2, 4, 10$  m) at the embedded length of  $L = 30$  m when the lateral displacement at the mudline is  $0.5D$ . It can be seen that under lateral loading, the shallow soil in front of monopiles with different aspect ratios exhibits significant uplift. In contrast, the soil behind the piles undergoes corresponding settlement. For flexible piles, as depicted in Fig. 11(a), the failure modes include shallow wedge failure and deep flow failure, with no notable bending and rotational deformation at the pile ends. The lateral load applied at the pile head is primarily resisted by the soil within  $0.4L$  depth, and the bottom soil hardly participates in bearing the lateral load. However, as illustrated in Fig. 11(b)-(c), as the aspect ratio decreases, monopiles gradually exhibit characteristics of semi-rigid or rigid piles. The resistance of the pile is increasingly provided by the deeper soil, and a significant reverse kick can be observed at the pile ends, meaning that the shear force and moment at the pile ends correspondingly contribute to the lateral resistance of the monopile. When the aspect ratio  $L/D$  is 3, only wedged and rotation failure modes are observed under lateral loads. Large-diameter monopiles clearly rotate around a certain point near the bottom, and these two failure mechanisms become particularly pronounced, showing a completely different failure mode from that of small-diameter flexible piles. This indicates that the failure modes of monopiles significantly change with variations in the aspect ratio  $L/D$ , which inevitably affects the lateral load characteristics of the monopile. However, this aspect is overlooked in the traditional  $p$ - $y$  method and should be considered in the

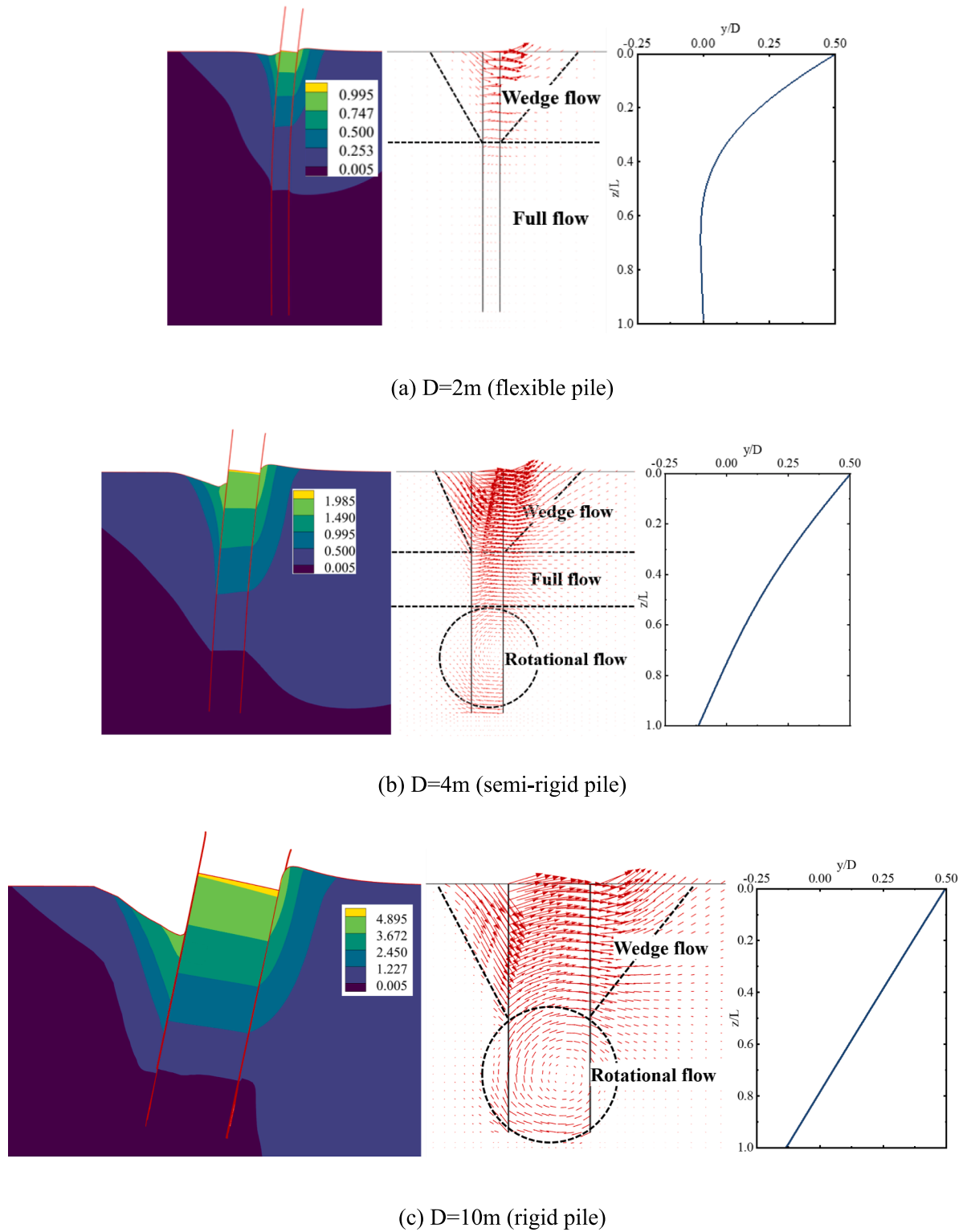


Fig. 11. Failure modes of monopiles of different diameters.

lateral load analysis of large-diameter monopiles.

#### 4.2. Quantification of the contribution of four soil reactions

Fig. 1(c) presents the four-spring soil reaction model with the one-dimensional (1D) finite-element program, in which the monopile has been discretized using the two-node Timoshenko beam elements. Similarly, the soil elements adopt interpolation functions identical to the

beam element, as described by Burd et al. (2020). These elements are attached to the pile element across the entire pile, thereby enabling a comprehensive representation of pile-soil interaction. Additionally, the soil reaction curves are also crucial in characterizing the nonlinearity of the soil around the pile.

A common method currently used to obtain  $p$ - $y$  curves involves fitting the pile moment obtained from experiments or numerical simulations to a specific function. Following this approach, distributed lateral



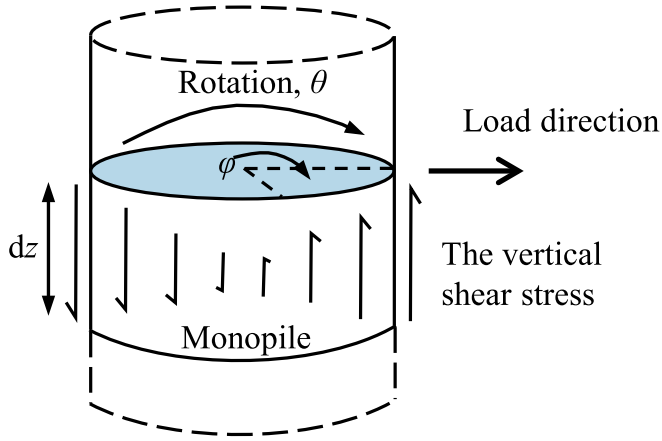


Fig. 12. Distribution of shear stress at the interface between the monopile and soil (Byrne et al., 2020a).

soil reaction and deformation along the pile are then calculated using Eq. (6) and (7) by double integration and differentiation at different depths. In this study, the method employed to determine the  $p$ - $y$  curve involves extracting the normal stresses at the pile-soil interface and the lateral deformation of the pile shaft at the corresponding depth.

$$y = \int \left( \int \phi dz \right) dz = \int \left( \int \frac{M}{EI} dz \right) dz \quad (6)$$

$$p = -\frac{d^2 M}{dz^2} \quad (7)$$

It is evident that the pile moment calculated by the first method includes both the moment  $M_p$  generated by the distributed lateral load and the distributed moment  $m$  generated by the pile side friction, as shown in Eq. (8). However, this approach has its limitations. Therefore, this method tends to overestimate the distributed lateral load. Moreover, since the distributed moment  $m$  is associated with the rotation angle of the pile shaft rather than the lateral displacement, the obtained  $p$ - $y$  curves are not the actual  $p$ - $y$  curves (Maatouk et al., 2022), and consequently, this discrepancy leads to inaccuracies in quantifying the contributions of each component.

$$M = M_p + M_m = \int p dz dz + \int m dz \quad (8)$$

The correlation between the distributed moment  $m$  and the pile side shear stress  $t_z$  on the cross-section of the monopile is as follows:

$$m = \int_0^{2\pi} t_z D^2 \cos \theta d\theta \quad (9)$$

The vertical shear stress  $t_z$  and the variable  $\theta$  are shown in Fig. 12.

To determine the base shear and moment soil reaction curves, one must integrate the soil unit stresses in the soil layer at the base of the monopile.

Fig. 13 illustrates the load-displacement response calculated on the basis of the 1D model by applying the  $p$ - $y$  curves generated from the FEM results and the API standard. Contrasted with the response of the FEM, the API method severely overestimates the lateral resistance of monopiles for piles ( $L/D = 3$  and  $7.5$ ). In contrast, for the extracted soil reaction curves, if only the distributed lateral load ( $p$ ) is used, the lateral bearing capacity of monopiles would be underestimated. However, with the additional consideration of distributed moment ( $m$ ), and base shear force ( $H$ ), and base moment ( $M$ ), the load-displacement response of monopiles with different  $L/D$  ratios can be more reasonably predicted. Based on the four types of soil reaction curves extracted, the contributions of distributed lateral load, distributed moment, base shear force, and base moment to the lateral resistance of large-diameter monopiles with varied relative densities (parameters as in Section 4.6) have been quantified, as illustrated in Fig. 14. It can be seen that variations in the parameters of the soils (higher or lower stiffness) have essentially no effect on the contribution of the soil reaction components in a given length-to-diameter ratio monopile. The contribution of the soil reaction force component is mainly related to the  $L/D$  ratio, and this conclusion is similar to the results of Burd et al. (2020). In addition, it is observed that apart from the distributed lateral load, among the other three types of soil reaction components, the contribution of the distributed moment is the largest (reaching 14 %), followed by base shear force (reaching 5 %), while the effect of the base moment is minimal. Therefore, it is suggested that the lateral resistance response of large-diameter monopiles should consider not only the effects of distributed lateral load but also the influence of distributed moments. Given the negligible contribution of base shear force and base moment, which can be disregarded, this paper recommends utilizing the ' $p$ - $y + m$ - $\theta$ ' model. The subsequent sections will focus only on examining two soil reaction curves: distributed moment and distributed lateral load.

#### 4.3. Determination of soil reaction curves

Typical soil reaction models consist of three components: the curve function, the initial stiffness, and the ultimate soil reaction. The common shapes of curves include the hyperbolic tangent function, the parabolic function, and the hyperbolic function.

The API standard employs the  $p$ - $y$  curve formula developed by

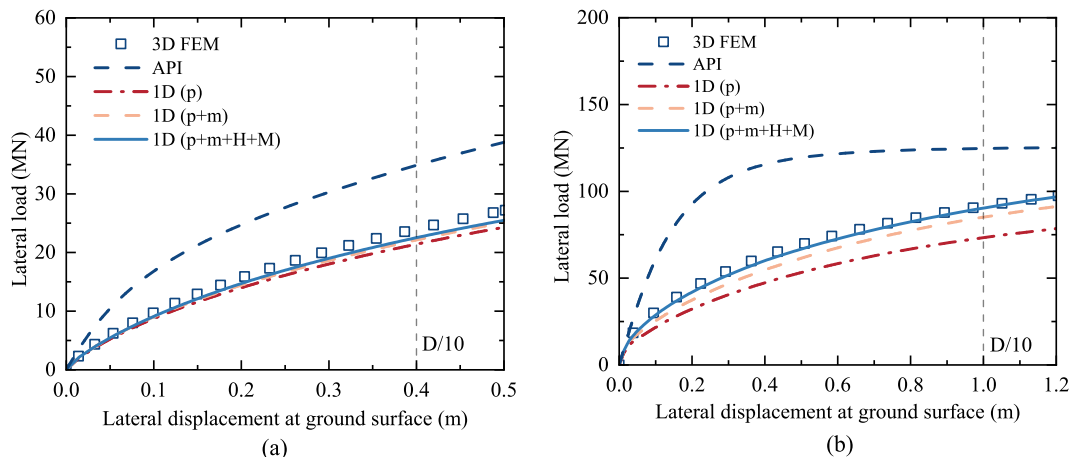


Fig. 13. Load-displacement curves of 1D model (a)  $D = 4$  m,  $L/D = 7.5$  (b)  $D = 10$  m,  $L/D = 3$ .

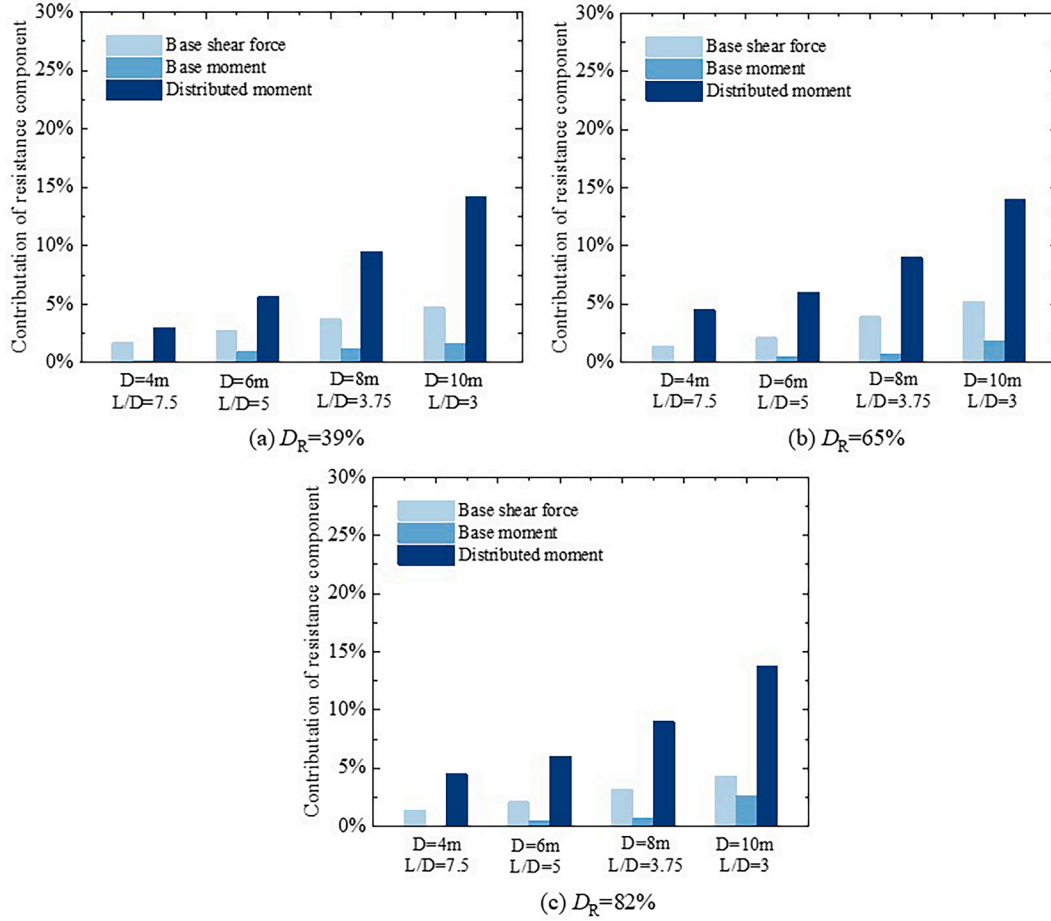


Fig. 14. Contribution of the soil reaction components to the lateral resistance response of monopiles with varied relative densities.

Table 6

Dimensionless formulas for the soil reaction curves (Burd et al., 2020).

Normalized variables	Dimensionless form
Distributed lateral load, $p$	$\frac{p}{\sigma_v D}$
Distributed moment, $m$	$\frac{m}{ p D}$
Base shear force, $H$	$\frac{H}{\sigma_v D^2}$
Base moment, $M$	$\frac{M}{\sigma_v D^3}$
Lateral displacement, $y$	$\frac{yG_0}{\sigma_v D}$
Pile cross-section rotation, $\theta$	$\frac{\theta G_0}{\sigma_v}$

O'Neill and Murchison (1983) from the laterally loaded pile experiments. This formulation is described using a tangent hyperbolic function as follows:

$$p(y, z) = Ap_u \tanh\left(\frac{k_{API} z}{Ap_u} y\right) \quad (10)$$

Where  $k_{API}$  represents the initial stiffness,  $p_u$  represents the ultimate soil reaction, and  $A$  is the depth correction factor for the soil reaction.

The PISA model thoroughly accounts for four types of soil reactions and accurately depicts complex pile-soil interactions. The soil reaction and deformation variables in the PISA model are dimensionless, as detailed in Table 6, with each soil reactions represented by a four-parameter conic function in Eq. (11).

$$-n\left(\frac{\bar{y}}{\bar{y}_u} - \frac{\bar{x}}{\bar{y}_u}\right) + (1-n)\left(\frac{\bar{y}}{\bar{y}_u} - \frac{\bar{x}k}{\bar{y}_u}\right)\left(\frac{\bar{y}}{\bar{y}_u} - 1\right) = 0 \quad (11)$$

Where  $n$  is the parameter that controls the degree of nonlinearity,  $k$  is the dimensionless initial stiffness of the curve,  $\bar{y}$  and  $\bar{y}_u$  are the dimensionless soil reactions and the ultimate soil reactions, respectively.  $\bar{x}$  and  $\bar{x}_u$  are the normalized deformation and the deformation corresponding to the ultimate soil reaction.

Furthermore, based on centrifuge experiments, Klinkvort and Hededal (2014) suggested a hyperbolic formulation curve shape different from the API and DNV standards, as shown in Eq. (12). The hyperbolic function can determine the soil reaction curve with only two parameters: the ultimate soil reaction force and the initial stiffness. This reduces the number of parameters by half compared to the four-parameter conic function suggested by the PISA model, simplifying the model and facilitating engineering design and secondary calibration based on specific site conditions. Thus, this paper proposes that the hyperbolic functions can be used to describe the two soil reaction curves, as shown in Eq. (12).

$$\bar{p} = \frac{\bar{y}}{(1/k) + (\bar{y}/\bar{p}_u)} \quad (12)$$

#### 4.4. Distributed lateral load

Fig. 15 shows the relationship curves of the normalized distributed lateral load and the normalized lateral deformation at depths of  $z = 0.35L$  and  $z = 0.90L$ , as calculated through finite element analysis. The figures illustrate that the  $p$ - $y$  curve for various diameters at the two depths is largely identical, suggesting minimal impact from the pile

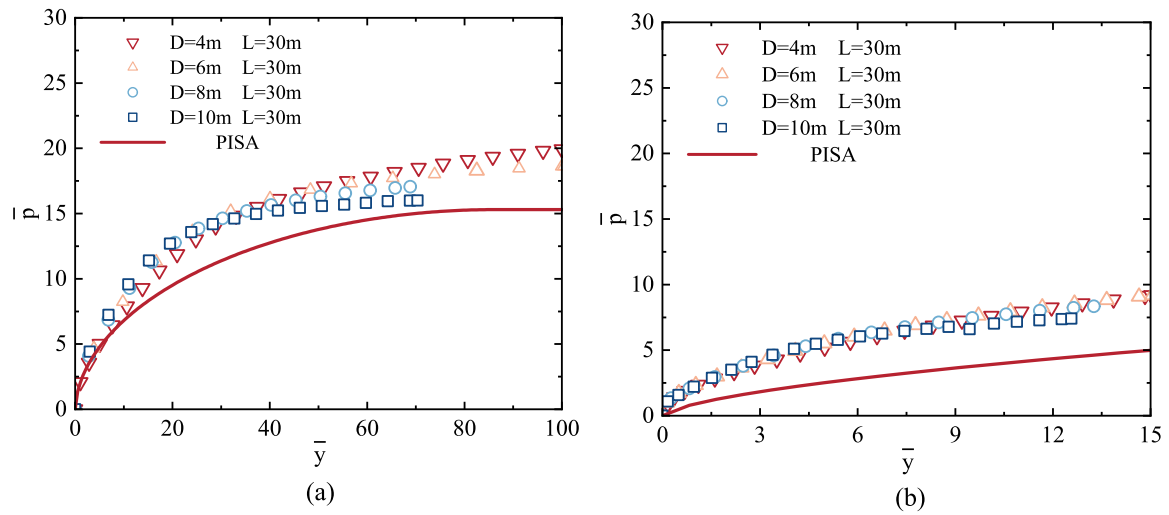


Fig. 15. Normalized distributed lateral load soil reaction curves (a)  $z/L = 0.35$  (b)  $z/L = 0.9$ .

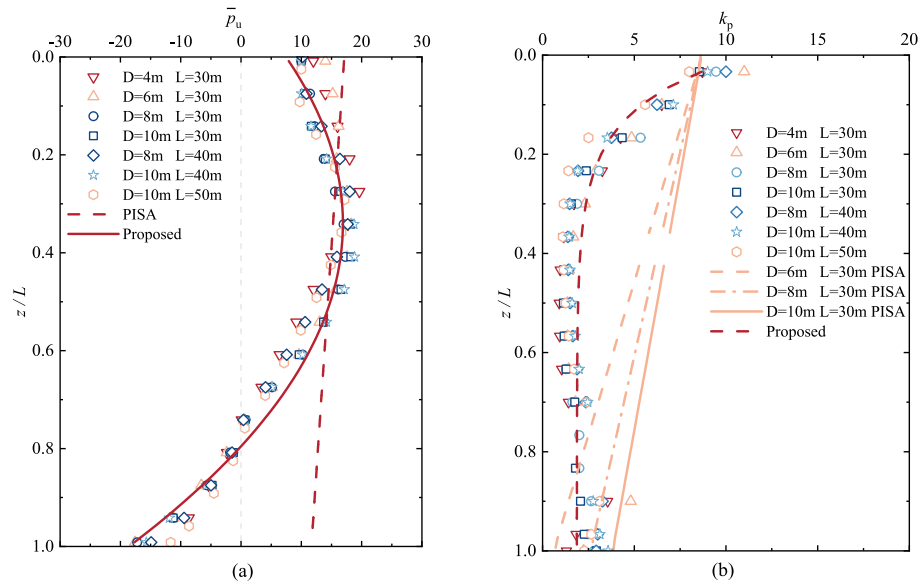


Fig. 16. Relationship between the normalized  $p$ - $y$  curve parameters and  $z/L$  (a) ultimate response parameter  $\bar{p}_u$  (b) initial stiffness parameter  $k_p$ .

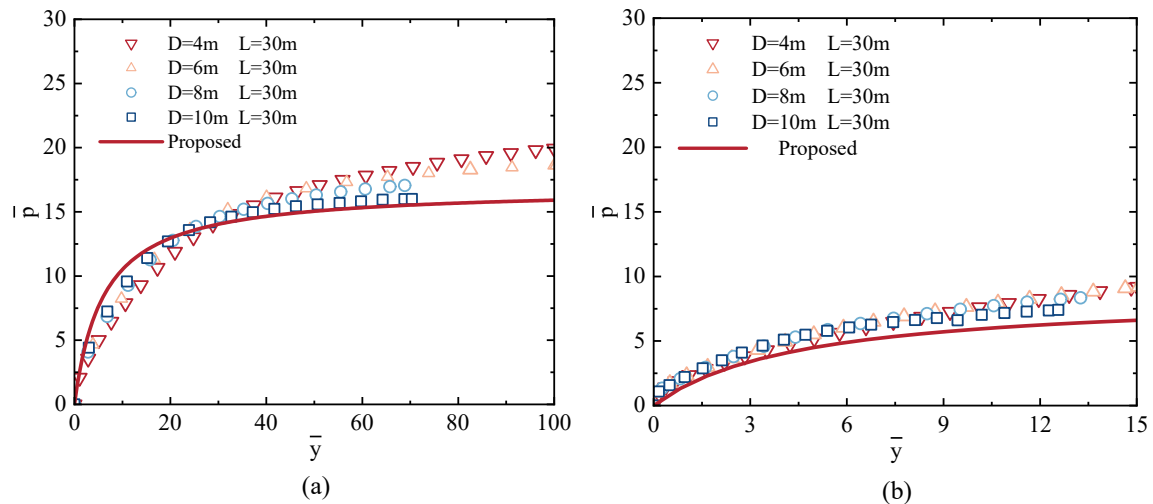


Fig. 17. Normalized distributed lateral load soil reaction curves (a)  $z/L = 0.35$  (b)  $z/L = 0.9$ .

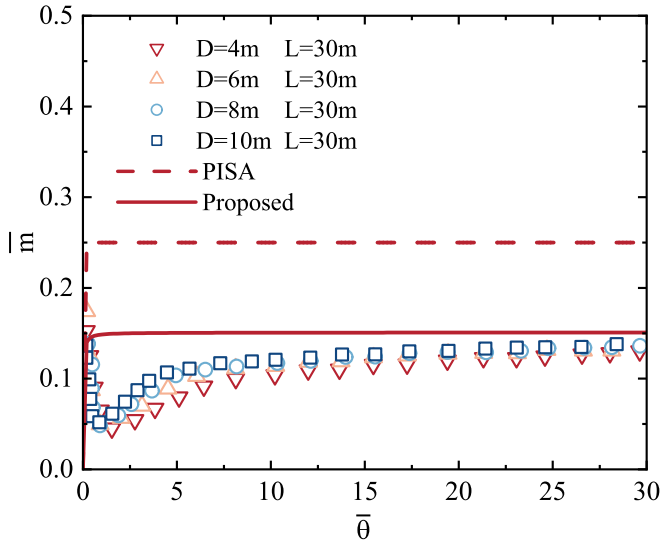


Fig. 18. Normalized distributed moment soil reaction curves ( $z/L = 0.35$ ).

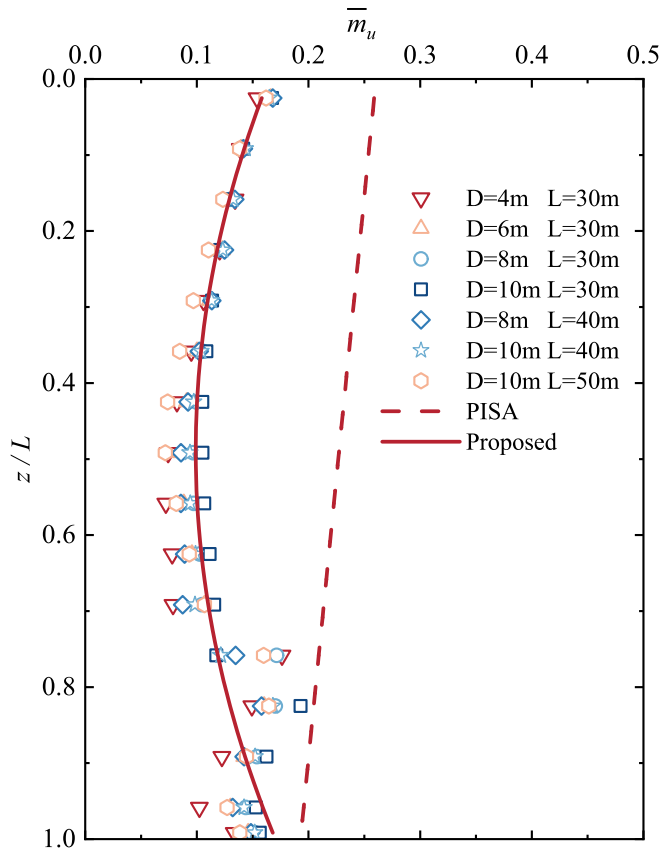


Fig. 19. Depth variations of the normalized ultimate distributed moment.

diameter. However, while the PISA model accurately represents the earlier stage of the  $p$ - $y$  curves, it tends to underestimate the ultimate resistance in the middle and later stages, which is consistent with the description of the PISA project.

To further analyze the influence of diameter on soil reaction curves, Fig. 16(a) illustrates the association of the normalized ultimate distributed lateral load of monopiles for the different diameters and embedded lengths with the normalized depth  $z/L$ . It reveals that for monopiles of the same diameter, embedded length, and aspect ratio (whether rigid or semi-rigid), the distribution profile along the pile length remains remarkably consistent, regardless of variations in pile diameter and embedded length. Notably, the ultimate distributed lateral load  $\bar{p}_u$  of the wedge zone experiences an increase with depth, peaking near  $z = 0.4L$  before gradually decreasing to a critical point around  $z = 0.8L$ . This trend is predominantly due to the change in the deformation mode of large-diameter monopiles, resulting in reduced relative deformation between the pile and soil near the rotation center, thereby hindering the mobilization of lateral soil reaction. In fact, the results of the PISA project also have the same patterns, but due to the mapping of the negative limiting lateral load below its center of rotation to the positive region, it is also difficult to find a suitable formula to describe the feature. It can also be seen from Fig. 16 that the PISA project uses a linear function to describe the distribution of  $\bar{p}_u$ , which also overestimates the ultimate lateral load  $\bar{p}_u$  near the center of rotation. Fig. 16 (a) also shows that the PISA model tends to overestimate the ultimate distributed lateral load near the center of rotation and fails to account for the depth-dependent variation in soil deformation mechanisms. The data in the figure was fitted with the least squares algorithm, leading to the adoption of the parabolic function described in Eq. (13) for capturing the depth variation, with the fitting results shown in Fig. 16. It becomes clear that the proposed parabolic function can accurately describe the distribution.

Although the API method is currently the industry standard, numerous experiments and numerical simulations have consistently shown that it tends to overestimate the initial stiffness. Poulos (1971) and Randolph (1981) demonstrated a close relationship between the initial stiffness and the small strain shear modulus of the soil. Therefore, this paper presents an analysis where the lateral deformation is normalized by the shear modulus, as shown in Table 6. Subsequently, the dimensionless initial stiffness  $k_p$  for monopiles with various diameters and embedded lengths is displayed in Fig. 16(b). This result reveals that the dimensionless initial stiffness  $k_p$  is remarkably uniform for monopiles with various diameters and embedded lengths, remaining consistent along the pile length. This paper also employs a parabolic function to describe the characteristic of higher initial stiffness  $k_p$  near the ground surface. From Fig. 16(b), it is apparent that the initial stiffness is minimally affected by the pile diameter, which is consistent with the research by Klinkvort (2012), Finn and Dowling (2015), and Wang et al. (2020).

Utilizing the methods for determining the normalized distributed lateral load and initial stiffness as proposed in Eq. (13) and (14), the normalized  $p$ - $y$  curves proposed in this paper are illustrated in Fig. 17. These curves effectively capture the  $p$ - $y$  curve characteristics for monopiles of different diameters and embedded lengths at various depths, offering a more precise reflection of the load-bearing response of monopiles.

**Table 7**  
Generalized plasticity model parameters for sand.

$D_R$	Elastic modulus				Plastic loading direction				Plastic modulus								
	$G_0$	$K_0$	$m_s$	$m_v$	$M_g$	$M_f$	$\alpha_g$	$\alpha_f$	$m_l$	$m_u$	$\gamma_{DM}$	$\gamma_d$	$\gamma_u$	$\beta_0$	$\beta_1$	$H_0$	$H_{u0}$
39 %	287	212	0.5	0.5	1.25	0.6	0.65	0.4	0.5	0.6	25	0.035	3.5	20	0.05	800	1200
82 %	364	269	0.5	0.5	1.28	1.01	0.85	0.42	0.5	0.6	25	0.035	3.5	10	0.055	1200	1300

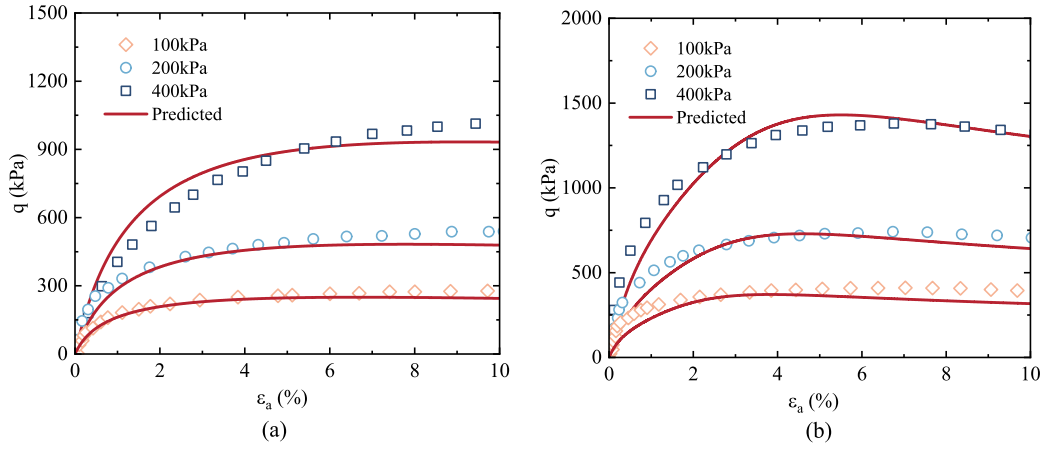


Fig. 20. Axial strain-deviatoric stress between simulations and measured data: (a)  $D_R = 39\%$ ; (b)  $D_R = 82\%$ .

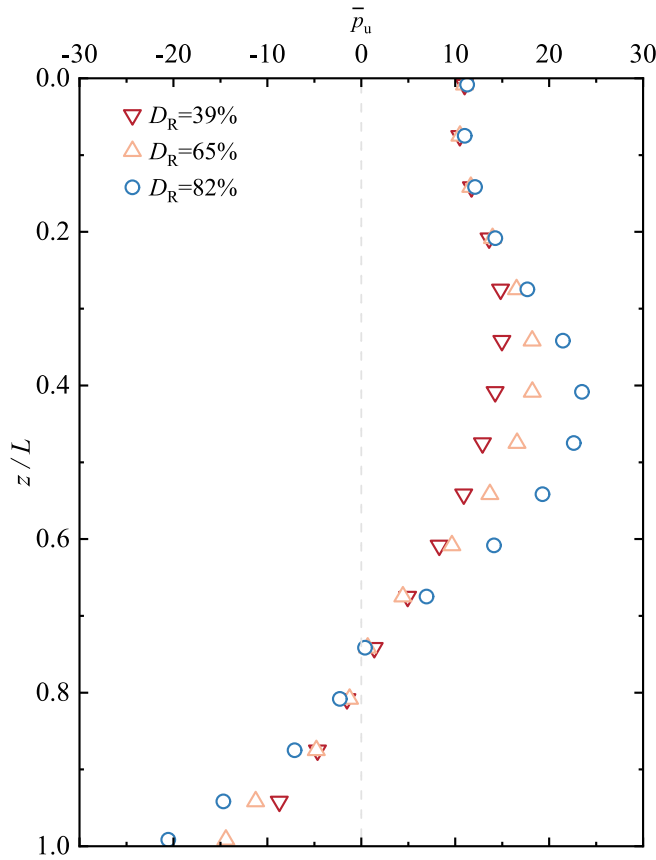


Fig. 21. Depth variations of the normalized ultimate distributed load of different relative densities.

$$\bar{p}_u = -81.5\left(\frac{z}{L}\right)^2 + 56.8\frac{z}{L} + 7 \quad (13)$$

$$k_p = 9.44e^{-6.83\frac{z}{L}} + 1.87 \quad (14)$$

#### 4.5. Distributed moment

From Eq. (9), it is evident that the distributed moment generated by the pile side shear stress primarily depends on two factors: the diameter and the magnitude of the pile side shear stress. Therefore, for small-diameter piles, the impact of the distributed moment can be assumed to be negligible, which is also consistent with the previously discussed

quantified proportion of distributed moment.

Fig. 18 illustrates the normalized soil reaction curve of the distributed moment. This figure indicates that their relationship, after normalization, is essentially consistent across various pile diameters. The initial value of the normalized distributed moment is high, and it gradually decreases with the rotation of the monopile. Subsequently, it increases again after reaching the minimum value, and finally, it tends to stabilize with the increase of the rotation angle. Fig. 19 illustrates the relationship of the ultimate distributed moment along the pile shaft. This figure demonstrates that the profile of the normalized ultimate distributed moment for piles of different diameters and embedded lengths is consistent, forming a parabolic distribution. Accordingly, a parabolic function is used for fitting, with the final results presented in Eq. (15). The method proposed in this paper, similar to PISA, is not affected by the diameter. In light of the accuracy of the calculation results and following the suggestions of Burd et al. (2020), an initial stiffness of  $k_m = 20$  is chosen, with the final fitting results being illustrated in Fig. 18.

$$\bar{m}_u = 0.167 + 0.274\left(\frac{z}{L}\right)^2 - 0.273\frac{z}{L} \quad (15)$$

#### 4.6. Effect of relative density

The aforementioned analyses were conducted on Toyoura sand, which is characterized by a relative density of 65%. To further enhance the applicability of the two types of soil reactions proposed in this paper, the 'p-y + m-θ' analysis model suitable for different relative densities of sand has been introduced. Systematic studies were carried out on monopiles with depth  $L = 30$  m and diameter  $D = 4$ –10 m. These studies focused on Toyoura sand with relative densities of 39% and 82%. The constitutive parameters for the above two relative densities of Toyoura sand were calibrated according to Example 2 and literature by Cen et al. (2018), with specific parameters listed in Table 7 and simulation results illustrated in Fig. 20.

Fig. 21 depicts the distribution profile of the ultimate distributed lateral load along the shaft of 10 m diameter monopiles across various relative densities. It reveals a trend in the distributed lateral load in proportion to the increase in relative density, which facilitates the establishment of a correlation between the normalized ultimate lateral load and relative density. Notably, for the normalized distributed lateral load, three depth-related variables show a significant linear correlation with relative density, as illustrated in Fig. 22. Moreover, the initial stiffness  $k_p$  after normalization is independent of relative density, so the results of different relative densities were combined for fitting, with the modified formulas shown in Eq. (16) to (20). The normalized distributed moment  $\bar{m}$ , being a function of the distributed lateral load  $p$ , is

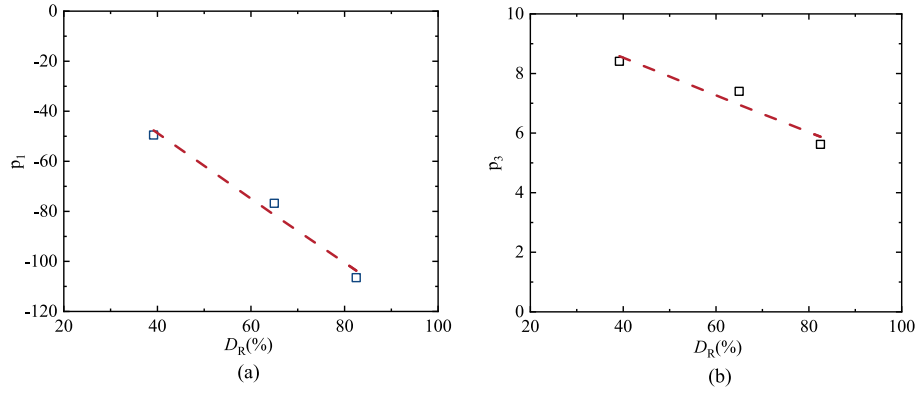


Fig. 22. Relationship between the normalized distributed lateral load parameters and relative density.

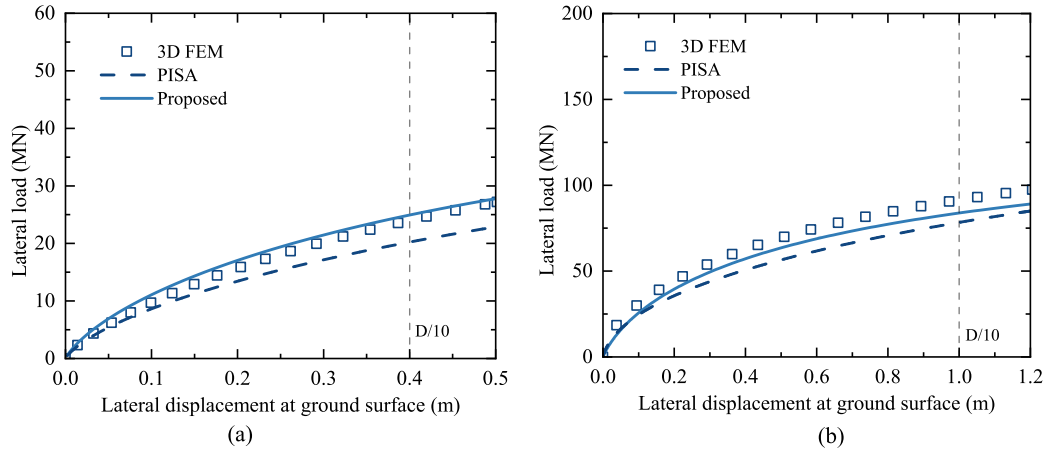


Fig. 23. Relationship between the measured load–displacement curves for monopiles and calculated results. (a)  $D = 4$  m,  $L/D = 7.5$  (b)  $D = 10$  m,  $L/D = 3$ .

**Table 8**  
Monopile specifications of the DTU 10 MW OWT.

Specifications	Value
Load eccentricity(m)	145
Diameter(m)	9
Embedded length(m)	45
Wall thickness(m)	0.1

fundamentally unaffected by relative density. Consequently, this paper simplifies the analysis by disregarding the impact of relative density on the normalized distributed moment, rendering the associated parameters independent of relative density.

$$\bar{p}_u = p_1 \left( \frac{z}{L} \right)^2 + p_2 \frac{z}{L} + p_3 \quad (16)$$

$$p_1 = 3.68 - 130.95D_R \quad (17)$$

$$p_2 = -16.67 + 113.08D_R \quad (18)$$

$$p_3 = 11.06 - 6.31D_R \quad (19)$$

$$k_p = 9.44e^{-6.83\frac{z}{L}} + 1.87 \quad (20)$$

To validate the performance of the soil reaction model proposed in this paper, comparisons were made between the predicted load–displacement curves for monopiles and the results derived from finite element results. As presented in Fig. 23, it is evident that the proposed soil reaction model agrees well with the response of the finite

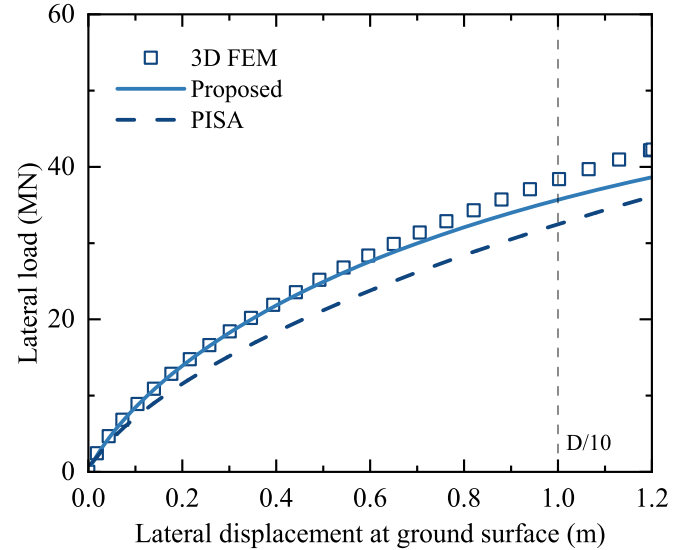


Fig. 24. Relationship between the measured load–displacement curves for monopiles and calculated results.

element method, demonstrating its performance in predicting the lateral loading behavior of large-diameter monopiles. To verify our model under varied eccentricities to ensure its broader applicability, we chose the monopile support system of DTU 10 MW OWT designed by Yang et al. (2020) for higher eccentricity simulations in the Toyoura sand with



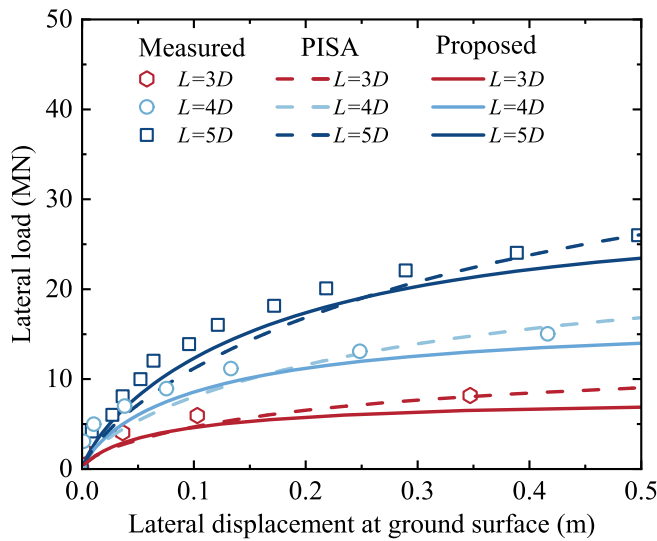


Fig. 25. Relationship between the measured load–displacement curves for monopiles (Maatouk et al., 2022) and calculated results.

a relative density of 82 %, with the monopile specifications shown in Table 8. The simulation results in Fig. 24 show that even with the higher eccentricity, the error in the calculation results is less than 6 %, which proves that our soil reaction model is still robust and valid and thus confirms its utility in a wider range of practical scenarios.

## 5. Validation of the applicability of the proposed model

To validate the performance of the newly developed ' $p-y + m-\theta$ ' model based on a two-parameter soil reaction curve proposed in this paper and to ensure consistency with the aspect ratio of offshore wind turbine monopile foundations, centrifuge tests with three different embedded lengths were selected (Maatouk et al., 2022). The sand was NE34 Fontainebleau sand, characterized by a relative density of 82 %. The effective weight of the sand was 10.27 kN/m<sup>3</sup>. The piles have an identical diameter ( $D = 5$  m) with various  $L/D$  ratios ( $L/D = 3, 4$  and  $5$ ). The monopiles were modeled using aluminum pipes, with an elastic modulus of 72.5 GPa and a thickness of 0.25 m in the prototype. In these tests, the lateral load was imposed uniformly across all monopiles at a load eccentricity of 25 m above the ground surface. Fig. 25 illustrates the load–displacement response of the test monopile, showcasing the capability of this method in predicting the lateral load characteristics of the monopile. Furthermore, the model proposed in this paper has shown better performance than the PISA model (Burd et al., 2020) under certain circumstances.

## 6. Conclusion

Considering that the  $p-y$  curves suggested by API standard are not proper for the lateral load analysis of large-diameter monopiles and that the four-parameter soil reaction curve of the PISA model is complex and does not account for the impact of the rotational deformation mode on the ultimate distributed lateral soil resistance. This paper quantifies the contributions of four soil reactions, establishes a ' $p-y + m-\theta$ ' model based on a two-parameter soil reaction curve, and validates it through

centrifuge tests. Considering the analysis discussed previously, we can infer the following conclusions:

(1) It is evident that apart from the distributed lateral load, the contribution of the distributed moment is the greatest (up to 14 %) in sand, followed by the base shear force (up to 5 %). The influence of the base moment is the least significant, and the contribution of these three types of soil reaction tends to increase with the decreasing length-diameter ratio. Therefore, in the lateral load analysis of large-diameter monopiles, the impact of distributed lateral load should not be the only consideration; the role of distributed moment should also be considered, while the contributions of base shear force and base moment are minor and can be neglected.

(2) The PISA model does not consider the impact of rotational deformation modes on ultimate distributed lateral soil resistance. This paper adopts the concept of parabolic fitting, suggesting that the distribution of ultimate lateral soil resistance should also consider the impact of rotational deformation modes of large-diameter monopiles. The recommended two-parameter soil reaction curve significantly reduces the parameters by half compared to the four-parameter conical function, making it more practical for engineering design.

(3) Among sands of different relative densities, the ultimate distributed lateral soil resistance shows a positive correlation with relative density. The three variables related to depth variation show a good linear relationship with relative density, whereas the normalized initial stiffness appears unrelated to relative density.

(4) The developed ' $p-y + m-\theta$ ' model has been confirmed by centrifuge tests as being effective for the lateral loading analysis of large-diameter monopiles. It accurately predicts the load–displacement relationship curve of monopiles. This method also has the potential to be further extended to the analysis of clays and layered soils to be applicable for lateral load analysis in the complex geological conditions of practical engineering projects.

## CRedit authorship contribution statement

**Xiuyang Zhang:** Writing – original draft, Validation, Software, Investigation, Formal analysis, Data curation. **Degao Zou:** Writing – review & editing, Software, Funding acquisition, Conceptualization. **Jingmao Liu:** Supervision, Methodology. **Kai Chen:** Supervision, Software. **Xin Li:** Investigation. **Tianju Wang:** Investigation.

## Declaration of competing interest

The authors declare that they have no known competing financial interests or personal relationships that could have appeared to influence the work reported in this paper.

## Data availability

Data will be made available on request.

## Acknowledgements

This work was supported by the National Natural Science Foundation of China (Grant Nos. 52192674, 52079023, U2240211, and 52109114). The writers would like to greatly acknowledge all the financial support and express their sincerest gratitude.

## Appendix

According to the plasticity theory, the strain increment can be defined as the sum of the elastic strain increment and the plastic strain increment, as follows:

$$d\epsilon = d\epsilon^e + d\epsilon^p \quad (A.1)$$

The correlation between stress and strain increments is shown below:

$$d\sigma' = D^{ep} : d\epsilon \quad (A.2)$$

The elasto-plastic stiffness matrix is expressed as:

$$D^{ep} = D^e - \frac{D^e : n_g : n^T : D^e}{H + n^T : D^e : n_g} \quad (A.3)$$

Where,  $D^e$  is the elasticity matrix;  $n_g$  is the plastic flow direction vector, representing the direction of the plastic strain increment.

The shear modulus and bulk modulus, taking into account the influence of stress dependence, are calculated as follows:

$$G = G_0 p_a (p'/p_a)^{m_v} \quad (A.4)$$

$$K = K_0 p_a (p'/p_a)^{m_s} \quad (A.5)$$

In the equation,  $p_a$  represents atmospheric pressure;  $m_v$  and  $m_s$  are model parameters;  $K_0$  and  $G_0$  are the coefficients of initial bulk modulus and shear modulus coefficient, respectively.

The following generalized expression is proposed for the stress-dilatancy relationship:

$$d_g = \frac{d\epsilon_v^p}{d\epsilon_s^p} = (1 + \alpha_g)(M_g - \eta) \quad (A.6)$$

In the formula,  $\epsilon_v^p$  and  $\epsilon_s^p$  are the plastic volumetric strain and the deviatoric strain, respectively; the critical stress ratio  $M_g$  is expressed by the Lode angle  $\theta$  and the friction angle  $\phi_g'$ :

$$M_g = \frac{6\sin\phi_g'}{3 + \sin\phi_g' \sin 3\theta} \quad (A.7)$$

The plastic flow direction vector  $n_g$  in triaxial space is then defined as follows:

$$n_g = (n_{gv}, n_{gs})^T = \left( \frac{d_g}{\sqrt{1 + d_g^2}}, \frac{1}{\sqrt{1 + d_g^2}} \right)^T \quad (A.8)$$

The loading direction vector  $n_f$  is expressed as:

$$n_f = (n_{fv}, n_{fs})^T = \left( \frac{d_f}{\sqrt{1 + d_f^2}}, \frac{1}{\sqrt{1 + d_f^2}} \right)^T \quad (A.9)$$

The definition of  $d_f$  is:

$$d_f = (1 + \alpha_f)(M_f - \eta) \quad (A.10)$$

The plastic modulus under loading and reloading conditions are determined as:

$$H_L = H_0 \cdot p_a \cdot (p/p_a)^{m_l} \cdot H_f \cdot (H_v + H_s) \cdot H_{DM} \cdot H_{den} \quad (A.11)$$

$$H_f = (1 - \eta/\eta_f)^4 \quad (A.12)$$

$$\eta_f = (1 + 1/\alpha_f)M_f \quad (A.13)$$

$$H_v = 1 - \eta/M_g \quad (A.14)$$

$$H_s = \beta_0 \beta_1 \exp(-\beta_0 \xi) \quad (A.15)$$

$$H_{DM} = \exp((1 - \eta/\eta_{\max})\gamma_{DM}) \quad (A.16)$$

$$\xi = \int |d\epsilon_s| \quad (A.17)$$

$$H_{den} = \exp(\gamma_d \epsilon_v) \quad (A.18)$$

where  $H_0$  is the plastic modulus;  $H_f$ ,  $H_v$ , and  $H_s$  are plastic coefficients; and  $\beta_0$ ,  $\beta_1$ , and  $\gamma_{DM}$  are model parameters.

The plastic modulus under unloading is defined as:

$$H_u = \begin{cases} H_{u0} (\eta_u/M_g)^{-\gamma_u} & |\eta_u/M_g| < 1 \\ H_{u0} & |\eta_u/M_g| \geq 1 \end{cases} \quad (A.19)$$

$$H_u = H_{u0} |\eta_u/M_g| \geq 1 \quad (A.20)$$

The model parameters  $m_u$ ,  $r_u$ , and  $H_{u0}$  are constants.

## References

- Achmus, M., Thieken, K., 2010. On the behavior of piles in non-cohesive soil under combined horizontal and vertical loading. *Acta Geotech.* 5, 199–210. <https://doi.org/10.1007/s11440-010-0124-1>.
- Amar Bouzid, D., 2018. Numerical investigation of large-diameter monopiles in sands: critical review and evaluation of both API and newly proposed py curves. *Int. J. Geomech.* 18 (11), 4018141. [https://doi.org/10.1061/\(ASCE\)GM.1943-5622.0001204](https://doi.org/10.1061/(ASCE)GM.1943-5622.0001204).
- API (American Petroleum Institute), 2021. Geotechnical and Foundation Design Considerations. API RP 2GEO, Washington, DC.
- Ashour, M., Helal, A., 2014. Contribution of vertical skin friction to the lateral resistance of large-diameter shafts. *J. Bridge Eng.* 19 (2), 289–302. [https://doi.org/10.1061/\(ASCE\)BE.1943-5592.0000505](https://doi.org/10.1061/(ASCE)BE.1943-5592.0000505).
- Burd, H.J., Taborda, D.M.G., Zdravković, L., Abadie, C.N., Byrne, B.W., Houlsby, G.T., Gavin, K.G., Igoe, D.J.P., Jardine, R.J., Martin, C.M., Mcadam, R.A., Pedro, A.M.G., Potts, D.M., 2020. PISA design model for monopiles for offshore wind turbines: Application to a marine sand. *Géotechnique* 70 (11), 1048–1066. <https://doi.org/10.1680/jgeot.18.P.277>.
- Byrne, B.W., Houlsby, G.T., Burd, H.J., Gavin, K.G., Igoe, D.J., Jardine, R.J., Martin, C.M., Mcadam, R.A., Potts, D.M., Taborda, D.M., 2020a. PISA design model for monopiles for offshore wind turbines: application to a stiff glacial clay till. *Géotechnique* 70 (11), 1030–1047. <https://doi.org/10.1680/jgeot.18.P.255>.
- Byrne, B.W., Mcadam, R.A., Burd, H.J., Beuckelaers, W.J., Gavin, K.G., Houlsby, G.T., Igoe, D.J., Jardine, R.J., Martin, C.M., Muir Wood, A., 2020b. Monotonic laterally loaded pile testing in a stiff glacial clay till at cowden. *Géotechnique* 70 (11), 970–985. <https://doi.org/10.1680/jgeot.18.PISA.003>.
- Cao, G., Ding, X., Yin, Z., Zhou, H., Zhou, P., 2021. A new soil reaction model for large-diameter monopiles in clay. *Comput. Geotech.* 137, 104311. <https://doi.org/10.1016/j.compgeo.2021.104311>.
- Cen, W.J., Luo, J.R., Bauer, E., Zhang, W.D., 2018. Generalized plasticity model for sand with enhanced state parameters. *J. Eng. Mech.* 144 (12), 4018108. [https://doi.org/10.1061/\(ASCE\)JEM.1943-7889.0001534](https://doi.org/10.1061/(ASCE)JEM.1943-7889.0001534).
- Chen, Z., Zhang, Z., Li, W., Wang, T., Zhang, J., 2023. Numerical study on the base shear force-displacement relationship for laterally loaded monopiles in dense sand. *Ocean Eng.* 286, 115527. <https://doi.org/10.1016/j.oceaneng.2023.115527>.
- Chen, K., Zou, D., Tang, H., Liu, J., Zhuo, Y., 2021. Scaled boundary polygon formula for cosserat continuum and its verification. *Eng. Anal. Bound. Elem.* 126, 136–150. <https://doi.org/10.1016/j.enganabound.2021.02.007>.
- Chen, K., Zou, D., Liu, J., Zhuo, Y., 2023. A high-precision formula for mixed-order polygon elements based on SBFEM. *Comput. Geotech.* 155, 105209. <https://doi.org/10.1016/j.compgeo.2022.105209>.
- Choo, Y.W., Kim, D., 2016. Experimental development of the p-y relationship for large-diameter offshore monopiles in sands: centrifuge tests. *J. Geotech. Geoenviron. Eng.* 142 (1), 4015058. [https://doi.org/10.1061/\(ASCE\)GT.1943-5606.0001373](https://doi.org/10.1061/(ASCE)GT.1943-5606.0001373).
- DNVGL, 2021. DNVGL-ST-0126-Support Structures for Wind Turbines. Det Norske Veritas, Greater Oslo.
- Finn, W.L., Dowling, J., 2015. Modelling effects of pile diameter. *Can. Geotech. J.* 53 (1), 173–178. <https://doi.org/10.1139/cgj-2015-0119>.
- Fu, D., Zhang, Y., Aamodt, K.K., Yan, Y., 2020. A multi-spring model for monopile analysis in soft clays. *Mar. Struct.* 72, 102768. <https://doi.org/10.1016/j.marstruc.2020.102768>.
- Fuentes, W., Gil, M., Rivillas, G., 2021. A p-y model for large diameter monopiles in sands subjected to lateral loading under static and long-term cyclic conditions. *J. Geotech. Geoenviron. Eng.* 147 (2), 4020164. [https://doi.org/10.1061/\(ASCE\)GT.1943-5606.0002448](https://doi.org/10.1061/(ASCE)GT.1943-5606.0002448).
- Gong, J., Zou, D., Kong, X., Liu, J., Chen, K., 2020. A coupled meshless-SBFEM-FEM approach in simulating soil-structure interaction with cross-scale model. *Soil Dyn. Earthq. Eng.* 136, 106214. <https://doi.org/10.1016/j.soildyn.2020.106214>.
- Gong, J., Zou, D., Kong, X., Liu, J., Chen, K., 2021a. The simulation of high compressive stress and extrusion phenomenon for concrete face slabs in CFRDs under strong seismic loads. *Soil Dyn. Earthq. Eng.* 147, 106792. <https://doi.org/10.1016/j.soildyn.2021.106792>.
- Gong, J., Zou, D., Kong, X., Liu, J., Qu, Y., 2021b. An approach for simulating the interaction between soil and discontinuous structure with mixed interpolation interface. *Eng. Struct.* 237, 112035. <https://doi.org/10.1016/j.engstruct.2021.112035>.
- Gong, J., Zou, D., Kong, X., Wang, D., Liu, J., Yu, X., 2023. A meshfree large-deformation analysis method for geotechnical engineering based on the RBF field variable mapping technology. *Comput. Meth. Appl. Mech. Eng.* 416, 116377. <https://doi.org/10.1016/j.cma.2023.116377>.
- Guo, Y., Wang, H., Lian, J., 2022. Review of integrated installation technologies for offshore wind turbines: current progress and future development trends. *Energy Conv. Manag.* 255, 115319. <https://doi.org/10.1016/j.enconman.2022.115319>.
- GWEC (Global Wind Energy Council), 2023. Global Wind Report 2023. Brussels, Belgium: GWEC.
- He, R., Kaynia, A.M., 2024. Winkler spring coefficients for laterally loaded piles. *Comput. Geotech.* 170, 106264. <https://doi.org/10.1016/j.compgeo.2024.106264>.
- Hernandez-Estrada, E., Lastres-Danguillecourt, O., Robles-Ocampo, J.B., Lopez-Lopez, A., Sevilla-Camacho, P.Y., Perez-Sariñana, B.Y., Dorrego-Portela, J.R., 2021. Considerations for the structural analysis and design of wind turbine towers: a review. *Renew. Sustain. Energy Rev.* 137, 110447. <https://doi.org/10.1016/j.rser.2020.110447>.
- Hong, Y., He, B., Wang, L.Z., Wang, Z., Ng, C.W.W., Mašin, D., 2017a. Cyclic lateral response and failure mechanisms of semi-rigid pile in soft clay: centrifuge tests and numerical modelling. *Can. Geotech. J.* 54 (6), 806–824. <https://doi.org/10.1139/cgj-2016-0356>.
- Hong, Y., Koo, C.H., Zhou, C., Ng, C.W.W., Wang, L.Z., 2017b. Small strain path-dependent stiffness of toyoura sand: laboratory measurement and numerical implementation. *Int. J. Geomech.* 17 (1), 4016036. [https://doi.org/10.1061/\(ASCE\)GM.1943-5622.0000664](https://doi.org/10.1061/(ASCE)GM.1943-5622.0000664).
- Hu, Q., Han, F., Prezzi, M., Salgado, R., Zhao, M., 2022. Lateral load response of large-diameter monopiles in sand. *Géotechnique* 72 (12), 1035–1050. <https://doi.org/10.1680/jgeot.20.00002>.
- Jiang, J., Fu, C., Wang, S., Chai, W., Ou, X., Zhao, Y., Zhang, L., 2022. A simplified analytical method of lateral bearing capacity of rigid single pile considering all soil reactions in sand. *Int. J. Geomech.* 22 (7), 4022087. [https://doi.org/10.1061/\(ASCE\)GM.1943-5622.0002408](https://doi.org/10.1061/(ASCE)GM.1943-5622.0002408).
- Karapiperis, K., Gerolymos, N., 2014. Combined loading of caisson foundations in cohesive soil: finite element versus winkler modeling. *Comput. Geotech.* 56, 100–120. <https://doi.org/10.1016/j.compgeo.2013.11.006>.
- Klinkvort, R.T., Hededal, O., 2014. Effect of load eccentricity and stress level on monopile support for offshore wind turbines. *Can. Geotech. J.* 51 (9), 966–974. <https://doi.org/10.1139/cgj-2013-0475>.
- Klinkvort, R.T., 2012. Centrifuge modelling of drained lateral pile - soil response: Application for offshore wind turbine support structures. Ph.D. Thesis, Technical University of Denmark.
- Lai, Y., Wang, L., Zhang, Y., Hong, Y., 2021. Site-specific soil reaction model for monopiles in soft clay based on laboratory element stress-strain curves. *Ocean Eng.* 220, 108437. <https://doi.org/10.1016/j.oceaneng.2020.108437>.
- Lai, Y., Li, W., He, B., Wang, L., Xiong, G., Liu, T., 2022. Centrifuge modelling of monotonic and cyclic lateral responses of a hybrid monopile-bucket foundation for offshore wind turbines. *Ocean Eng.* 260, 111967. <https://doi.org/10.1016/j.oceaneng.2022.111967>.
- Ling, H.I., Liu, H., 2003. Pressure-level dependency and densification behavior of sand through generalized plasticity model. *J. Eng. Mech.* 129, 851–860. [https://doi.org/10.1061/\(ASCE\)0733-9399\(2003\)129:8\(851\)](https://doi.org/10.1061/(ASCE)0733-9399(2003)129:8(851)).
- Liu, H., Wang, C., Ding, X., Zhang, Y., 2023. Comparative numerical analysis of the response of laterally loaded pile in coral and silica sands. *Acta Geotech.* 18 (9), 4767–4787. <https://doi.org/10.1007/s11440-023-01858-9>.
- Liu, J., Zou, D., Kong, X., 2020. A two-mechanism soil-structure interface model for three-dimensional cyclic loading. *Int. J. Numer. Anal. Methods Geomech.* 44 (15), 2042–2069. <https://doi.org/10.1002/nag.3118>.
- Liu, J., Zou, D., Ning, F., Kong, X., 2023. A unified constitutive model for instantaneous elastic-plastic and time-dependent creep behaviour of gravelly soils under complex loading. *Can. Geotech. J.* 60 (11), 1613–1628. <https://doi.org/10.1139/cgj-2022-0635>.
- Ma, Y., Yang, J., 2024. Lateral loading response of monopiles in sand considering installation effect. *Comput. Geotech.* 171, 106365. <https://doi.org/10.1016/j.compgeo.2024.106365>.
- Maatouk, S., Blanc, M., Thorel, L., 2022. Effect of embedding depth on the monotonic lateral response of monopiles in sand: centrifuge and numerical modelling. *Géotechnique* 1–16. <https://doi.org/10.1680/jgeot.22.00149>.
- Mcadam, R.A., Byrne, B.W., Houlsby, G.T., Beuckelaers, W.J.A.P., Burd, H.J., Gavin, K. G., Igoe, D.J.P., Jardine, R.J., Martin, C.M., Muir Wood, A., Potts, D.M., Skov Gretlund, J., Taborda, D.M.G., Zdravkovi C, L., 2020. Monotonic laterally loaded pile testing in a dense marine sand at Dunkirk. *Géotechnique* 70 (11), 986–998. <https://doi.org/10.1680/jgeot.18.PISA.004>.
- Murphy, G., Igoe, D., Doherty, P., Gavin, K., 2018. 3D FEM approach for laterally loaded monopile design. *Comput. Geotech.* 100, 76–83. <https://doi.org/10.1016/j.compgeo.2018.03.013>.
- Nie, X., Chen, K., Zou, D., Kong, X., Liu, J., Qu, Y., 2022. Slope stability analysis based on SBFEM and multistage polytree-based refinement algorithms. *Comput. Geotech.* 149, 104861. <https://doi.org/10.1016/j.compgeo.2022.104861>.
- Ning, F., Liu, J., Kong, X., Zou, D., 2020. Critical state and grading evolution of rockfill material under different triaxial compression tests. *Int. J. Geomech.* 20 (2), 4019154. [https://doi.org/10.1061/\(ASCE\)GM.1943-5622.0001550](https://doi.org/10.1061/(ASCE)GM.1943-5622.0001550).
- O'Neill, M.W., Murchison, J.M., 1983. An evaluation of py relationships in sands. University of Houston.
- Otsmane, L., Amar Bouzid, D., 2018. An Efficient FE model for SSI: Theoretical background and assessment by predicting the response of large diameter monopiles supporting OWECS. *Comput. Geotech.* 97, 155–166. <https://doi.org/10.1016/j.compgeo.2017.12.001>.
- Pastor, M., Zienkiewicz, O.C., Leung, K.H., 1985. Simple model for transient soil loading in earthquake analysis. II. Non-associative models for sands. *Int. J. Numer. Anal. Methods Geomech.* 9 (5), 477–498. <https://doi.org/10.1002/nag.1610090505>.
- Poulos, H.G., 1971. Behavior of laterally loaded piles: I-single piles. *J. Soil Mech. Found. Division* 97 (5), 711–731. <https://doi.org/10.1061/JSEFAQ.0001592>.
- Qu, Y., Zou, D., Chen, K., Liu, J., 2021. Three-dimensional refined analysis of seismic cracking and anti-seismic measures performance of concrete face slab in CFRDs. *Comput. Geotech.* 139, 104376. <https://doi.org/10.1016/j.compgeo.2021.104376>.
- Qu, Y., Zou, D., Liu, J., Yang, Z., Chen, K., 2022. Two-dimensional DEM-FEM coupling analysis of seismic failure and anti-seismic measures for concrete faced rockfill dam. *Comput. Geotech.* 151, 104950. <https://doi.org/10.1016/j.compgeo.2022.104950>.
- Randolph, M.F., 1981. The response of flexible piles to lateral loading. *Géotechnique* 31 (2), 247–259. <https://doi.org/10.1680/geot.1981.31.2.247>.
- Reese, L.C., Cox, W.R., Koop, F.R., 1974. Analysis of laterally loaded piles in sand. In: *Proceedings of the Offshore Technology Conference*, Paper No. 2080, pp. 473–483. Houston.

- Said, I.D., De Gennaro, V., Frank, R., 2009. Axisymmetric finite element analysis of pile loading tests. *Comput. Geotech.* 36 (1–2), 6–19. <https://doi.org/10.1016/j.compgeo.2008.02.011>.
- Song, C., Wolf, J.P., 1997. The scaled boundary finite-element method—alias consistent infinitesimal finite-element cell method—for elastodynamics. *Comput. Methods Appl. Mech. Eng.* 147, 329–355. [https://doi.org/10.1016/S0045-7825\(97\)00021-2](https://doi.org/10.1016/S0045-7825(97)00021-2).
- Sun, Y., Xu, C., Du, X., El Naggar, M.H., Zhang, X., Jia, J., 2020. Nonlinear lateral response of offshore large-diameter monopile in sand. *Ocean Eng.* 216, 108013. <https://doi.org/10.1016/j.oceaneng.2020.108013>.
- Taborda, D.M., Zdravković, L., Potts, D.M., Burd, H.J., Byrne, B.W., Gavin, K.G., Houlsby, G.T., Jardine, R.J., Liu, T., Martin, C.M., 2020. Finite-element modelling of laterally loaded piles in a dense marine sand at Dunkirk. *Géotechnique* 70 (11), 1014–1029. <https://doi.org/10.1680/jgeot.18.PISA.006>.
- Thieken, K., Achmus, M., Lemke, K., 2015. A new static p-y approach for piles with arbitrary dimensions in sand. *Geotechnik* 38, 267–288. <https://doi.org/10.1002/gete.201400036>.
- Truong, P., Lehane, B.M., 2018. Effects of pile shape and pile end condition on the lateral response of displacement piles in soft clay. *Géotechnique* 68 (9), 794–804. <https://doi.org/10.1680/jgeot.16.P.291>.
- Wan, X., Doherty, J.P., Randolph, M.F., 2021. Relationships between lateral and rotational load transfer stiffnesses and soil modulus for the elastic response of monopiles. *Comput. Geotech.* 137, 104256. <https://doi.org/10.1016/j.compgeo.2021.104256>.
- Wang, H., Wang, L.Z., Hong, Y., He, B., Zhu, R.H., 2020. Quantifying the influence of pile diameter on the load transfer curves of laterally loaded monopile in sand. *Appl. Ocean Res.* 101, 102196. <https://doi.org/10.1016/j.apor.2020.102196>.
- Wang, H., Wang, L., Hong, Y., Askarinejad, A., He, B., Pan, H., 2021a. Influence of pile diameter and aspect ratio on the lateral response of monopiles in sand with different relative densities. *J. Mar. Sci. Eng.* 9 (6), 618. <https://doi.org/10.3390/jmse9060618>.
- Wang, H., Wang, L., Hong, Y., Mašin, D., Li, W., He, B., Pan, H., 2021b. Centrifuge testing on monotonic and cyclic lateral behavior of large-diameter slender piles in sand. *Ocean Eng.* 226, 108299. <https://doi.org/10.1016/j.oceaneng.2020.108299>.
- Wang, H., Fraser Bransby, M., Lehane, B.M., Wang, L., Hong, Y., 2022a. Numerical investigation of the monotonic drained lateral behaviour of large-diameter rigid piles in medium-dense uniform sand. *Géotechnique* 1–12. <https://doi.org/10.1680/jgeot.21.00149>.
- Wang, H., Lehane, B.M., Bransby, M.F., Askarinejad, A., Wang, L.Z., Hong, Y., 2022b. A simple rotational spring model for laterally loaded rigid piles in sand. *Mar. Struct.* 84, 103225. <https://doi.org/10.1016/j.marstruc.2022.103225>.
- Wang, H., Wang, L.Z., Askarinejad, A., Hong, Y., He, B., 2022c. Ultimate soil resistance of the laterally loaded pile in uniform sand. *Can. Geotech. J.* 60 (4), 587–593. <https://doi.org/10.1139/cgj-2021-0487>.
- Wu, X., Hu, Y., Li, Y., Yang, J., Duan, L., Wang, T., Adcock, T., Jiang, Z., Gao, Z., Lin, Z., Borthwick, A., Liao, S., 2019. Foundations of offshore wind turbines: A review. *Renew. Sustain. Energy Rev.* 104, 379–393. <https://doi.org/10.1016/j.rser.2019.01.012>.
- Yang, Y., Bashir, M., Li, C., Michailides, C., Wang, J., 2020. Mitigation of coupled wind-wave-earthquake responses of a 10 MW fixed-bottom offshore wind turbine. *Renew. Energy* 157, 1171–1184. <https://doi.org/10.1016/j.renene.2020.05.077>.
- Zdravković, L., Taborda, D.M.G., Potts, D.M., Abadías, D., Burd, H.J., Byrne, B.W., Gavin, K.G., Houlsby, G.T., Jardine, R.J., Martin, C.M., Mcadam, R.A., Ushev, E., 2020. Finite-element modelling of laterally loaded piles in a stiff glacial clay till at Cowden. *Géotechnique* 70 (11), 999–1013. <https://doi.org/10.1680/jgeot.18.PISA.005>.
- Zhang, Y., Andersen, K.H., 2019. Soil reaction curves for monopiles in clay. *Mar. Struct.* 65, 94–113. <https://doi.org/10.1016/j.marstruc.2018.12.009>.
- Zhang, X.D., Li, B.J., Yang, Z.X., Zhu, B.T., Xu, R.Q., Wang, J.C., Gong, X.N., 2023. Timoshenko beam theory-based analytical solution of laterally loaded large-diameter monopiles. *Comput. Geotech.* 161, 105554. <https://doi.org/10.1016/j.compgeo.2023.105554>.
- Zhang, J., Zhao, M., Eisenträger, S., Du, X., Song, C., 2022. An asynchronous parallel explicit solver based on scaled boundary finite element method using octree meshes. *Comput. Methods Appl. Mech. Eng.* 401, 115653. <https://doi.org/10.1016/j.cma.2022.115653>.
- Zhu, B., Sun, Y.X., Chen, R.P., Guo, W.D., Yang, Y.Y., 2015. Experimental and analytical models of laterally loaded rigid monopiles with hardening p-y curves. *J. Waterw. Port Coast. Ocean Eng.* 141 (6), 4015007. [https://doi.org/10.1061/\(ASCE\)WW.1943-5460.0000310](https://doi.org/10.1061/(ASCE)WW.1943-5460.0000310).
- Zhu, J., Yu, J., Huang, M., Shi, Z., Shen, K., 2022. Inclusion of small-strain stiffness in monotonic p-y curves for laterally loaded piles in clay. *Comput. Geotech.* 150, 104902. <https://doi.org/10.1016/j.compgeo.2022.104902>.
- Zhu, B., Zhu, Z., Li, T., Liu, J., Liu, Y., 2017. Field tests of offshore driven piles subjected to lateral monotonic and cyclic loads in soft clay. *J. Waterw. Port Coast. Ocean Eng.* 143 (5), 5017003. [https://doi.org/10.1061/\(ASCE\)WW.1943-5460.0000399](https://doi.org/10.1061/(ASCE)WW.1943-5460.0000399).
- Zou, D., Xu, B., Kong, X., Liu, H., Zhou, Y., 2013. Numerical simulation of the seismic response of the Zipingpu concrete face rockfill dam during the Wenchuan earthquake based on a generalized plasticity model. *Comput. Geotech.* 49, 111–122. <https://doi.org/10.1016/j.compgeo.2012.10.010>.